Visible–near-infrared observations of organics and carbonates on (101955) Bennu: Classification method and search for surface context

S.M. M Ferrone, B.E. E Clark, H.H. H Kaplan, J.-L. Rizos, X.-D. Zou, J.-Y. Li, M.A. A Barucci, A.A. A Simon, D. Reuter, P.H. H Hasselmann, et al.

Icarus 368 (2021) 114579

Contents lists available at ScienceDirect

Icarus

journal homepage: www.elsevier.com/locate/icarus

Research Paper

Visible–near-infrared observations of organics and carbonates on (101955) Bennu: Classification method and search for surface context

S.M. Ferrone [a,b,*], B.E. Clark [b], H.H. Kaplan [c], J.-L. Rizos [d], X.-D. Zou [e], J.-Y. Li [e], M.A. Barucci [b], A.A. Simon [c], D. Reuter [c], P.H. Hasselmann [b], J.D.P. Deshapriya [b], G. Poggiali [f], J.R. Brucato [f], S. Cambioni [g], Ed Cloutis [h], V.E. Hamilton [i], D.S. Lauretta [j]

[a] LESIA-Observatoire de Paris, Université PSL, CNRS, Université de Paris, Sorbonne Université, Paris, France
[b] Department of Physics and Astronomy, Ithaca College, Ithaca, NY, USA
[c] NASA Goddard Space Flight Center, Laurel, MD, USA
[d] Instituto de Astrofísica de Canarias, La Laguna, Tenerife, Spain
[e] Planetary Science Institute, Tucson, AZ, USA
[f] INAF-Astrophysical Observatory of Arcetri, Firenze, Italy
[g] Division of Geological and Planetary Sciences, California Institute of Technology, Pasadena, CA, USA
[h] Department of Geography, University of Winnipeg, Winnipeg, MB, Canada
[i] Southwest Research Institute, Boulder, CO, USA
[j] Lunar and Planetary Laboratory, University of Arizona, Tucson, AZ, USA

ARTICLE INFO

Keywords:
Bennu
Organics
Spectroscopy
OSIRIS-REx
Carbonates

ABSTRACT

The OSIRIS-REx Visible and InfraRed Spectrometer (OVIRS) onboard the Origins, Spectral Interpretation, Resource Identification, and Security–Regolith Explorer (OSIRIS-REx) spacecraft detected ~3.4-μm absorption features indicative of carbonates and organics on near-Earth asteroid (101955) Bennu. We apply a Kolmogorov-Smirnov similarity test to OVIRS spectra of Bennu and laboratory spectra of minerals to categorize 3.4-μm features observed on Bennu as representing either carbonates or organics. Among the 15,585 spectra acquired by OVIRS during high-resolution (4 to 9 m/spectrum footprint) reconnaissance observations of select locations on Bennu's surface, we find 544 spectral matches with carbonates and 245 spectral matches with organics (total of 789 high-confidence spectral matches). We map the locations of these matches and characterize features of Bennu's surface using corresponding image data. Image data are used to quantitatively characterize the albedo within each spectrometer footprint. We find no apparent relationships between spectral classification and surface morphological expression, and we find no correlation between carbon species classification and other spectral properties such as slope or band depth. This suggests either that carbonates and organics are ubiquitous across the surface of Bennu, independent of surface features (consistent with findings from laboratory studies of carbonaceous chondrites), or that the observations do not have the spatial resolution required to resolve differences. However, we find more organic spectral matches at certain locations, including the site from which the OSIRIS-REx mission collected a sample, than at others. Higher concentrations of organics may be explained if these materials have been more recently exposed to surface alteration processes, perhaps by recent crater formation.

1. Introduction

NASA's OSIRIS-REx mission (Lauretta et al., 2017, 2021) is returning a sample from near-Earth asteroid (101955) Bennu, a low-albedo 500-m-diameter body whose closest known analogs are the hydrated carbonaceous chondrite meteorites (Clark et al., 2011; Hamilton et al., 2019). In the spring of 2019, OSIRIS-REx conducted global observations at a range of 5 km with the OSIRIS-REx Visible and InfraRed Spectrometer (OVIRS) (Reuter et al., 2018) to map the composition of the surface (at ~20 m/spectrum footprint), including potential sites for sample collection (Lauretta et al., 2017, 2021; Simon et al., 2020a. Four candidate sample sites were selected by the mission for further study:

* Corresponding author at: LESIA-Observatoire de Paris, Université PSL, CNRS, Université de Paris, Sorbonne Université, Paris, France.
E-mail address: salvatore.ferrone@obspm.fr (S.M. Ferrone).

https://doi.org/10.1016/j.icarus.2021.114579
Received 3 March 2021; Received in revised form 20 May 2021; Accepted 5 June 2021
Available online 19 June 2021

Table 1
Regions of interest in this study, with associated coordinates, number of OVIRS spectra, and MapCam images where applicable. The Minokawa crater did not have corresponding MapCam images registered to the shape model at the time of writing.

Region of interest	Center coordinates (lon, lat [degrees])	Number of OVIRS spectra	MapCam image ID (if applicable)
Sandpiper	330 E, −55 S	1790	20191005T194606S042
Osprey	80 E, 15 N	3713	20191012T221058S857
Kingfisher	55 E, 15 N	3170	20191019T214213S359
Nightingale	60 E, 50 N	2169	20191026T212219S754
Minokawa (#6 in Deshapriya et al., 2021)	260 E, −15 S	647	n/a
Other observations of opportunity (included in "All Recon A" analyses)	50 E, −30 S 30 E, −20 S 135 E, 0 N 190 E, 10 N 340 E, 30 N	4096	n/a

Nightingale, Osprey, Kingfisher, and Sandpiper. These four regions of interest were targeted and characterized from a closer range of 1 km (4 to 9 m/spectrum footprint) in October 2019, in a mission phase called Reconnaissance (Recon) A, which also included observations of opportunity of some other areas on Bennu's surface (Table 1, Fig. 1).

Simon et al. (2020a) analyzed the global OVIRS data and mapped the distribution of carbon-bearing species, namely carbonates and organics (which are not separable at the lower areal resolution of the global dataset). Kaplan et al. (2020a) analyzed the higher-resolution Recon A data for Nightingale, the site that was ultimately sampled by OSIRIS-REx, and found evidence of specific carbonate minerals (calcite, dolomite, magnesite) distributed throughout the area and probably associated with bright veins visible in boulders seen in corresponding imaging data. These observations suggest that the parent body of asteroid Bennu experienced large-scale hydrothermal aqueous alteration in a chemically open system.

Although carbonates are found in low abundances in carbonaceous meteorites, they do not signal their presence spectroscopically. This indicates that the spectral detections reported by Kaplan et al. and Simon et al. must be related to a different scale of carbonate-forming process, which is not captured by our current knowledge of carbonaceous meteorites.

The results of Simon et al. (2020a) and Kaplan et al. (2020a) raise questions about the distributions and geomorphological occurrences of carbonates and organics on Bennu. Are spectrally separable organics and carbonates found at other locations on Bennu, in addition to Nightingale? Does the distribution of organics and/or carbonates on Bennu correlate with boulder properties such as albedo or roughness, or with other quantitative surface properties? Organics are known to be dark and spectrally red throughout the visible to near-infrared (Moroz et al., 2004). Are organics associated with spectrally red and dark locations on Bennu? Are the areas observed during Recon A distinct with respect to their carbonate and organic distributions? Our study uses the Recon A dataset to address these questions at sufficient spatial resolution.

Although correlating spectral observations to imaging data can be difficult due to projection effects (e.g. Ferrone et al., 2021a), spacecraft motion during integration, differences in viewing geometry (Zou et al., 2021), and differences in spatial resolution, we present our findings with respect to quantitative measures of surface properties independently observed within each OVIRS footprint by the MapCam medium-field imager of the OSIRIS-REx Camera Suite (OCAMS) (Rizk et al., 2018; Golish et al., 2020).

Due to the stretching of the C—H and C—O bonds, carbonate and organic features occur at roughly the same wavelengths, between approximately 3.2 and 3.6 μm, referred to hereafter as the 3.4-μm region (Alexander et al., 2007, 2014; Glavin et al., 2018; Kaplan et al., 2019; Kaplan et al., 2020a). Not much material is required to create an absorption feature because these absorption bands are attributed to fundamental C—H stretching and first order overtones: Kaplan et al. (2020a) show that less than 0.1 wt% of carbonates could impart a detectable absorption feature in a carbonate-poor reflectance spectrum of Bennu. Donaldson Hanna et al. (2019) showed that even a few weight

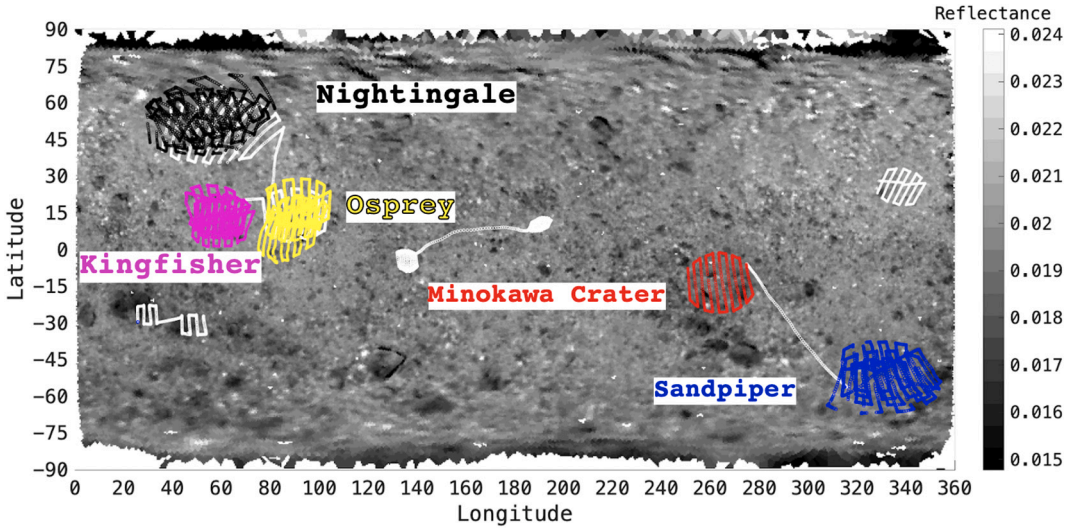

Fig. 1. Coverage map of the OSIRIS-REx Reconnaissance A mission phase observations obtained by the OVIRS spectrometer. The observation sequence surrounding Nightingale is black (60 E, 50 N), the region surrounding Kingfisher is pink (55 E, 15 N), the region surrounding Osprey is yellow (80 E, 15 N), the region encasing the Minokawa Crater is red (260 E, −15 N), and the Sandpiper region is blue (330 E, −55 N). The rest of the data set (observations of opportunity for context) are shown in white. The width of the lines (made up of observation spots) represents the diameter of the OVIRS spot projected onto Bennu's surface. The basemap shown is a global mosaic of images acquired during the Detailed Survey mission phase at ~5 cm/pixel (Bennett et al., 2021). The images were photometrically corrected to standard viewing geometry of incidence, emission, and phase equal to 30, 0, 30 degrees, respectively, using a Lommel-Seeliger photometric model (Golish et al., 2021). The coordinates of each pixel were registered to a global shape model (Barnouin et al., 2020), and corresponding reflectance values were averaged together per facet of the global shape model (0.8-m-sized facets). (For interpretation of the references to colour in this figure legend, the reader is referred to the web version of this article.)

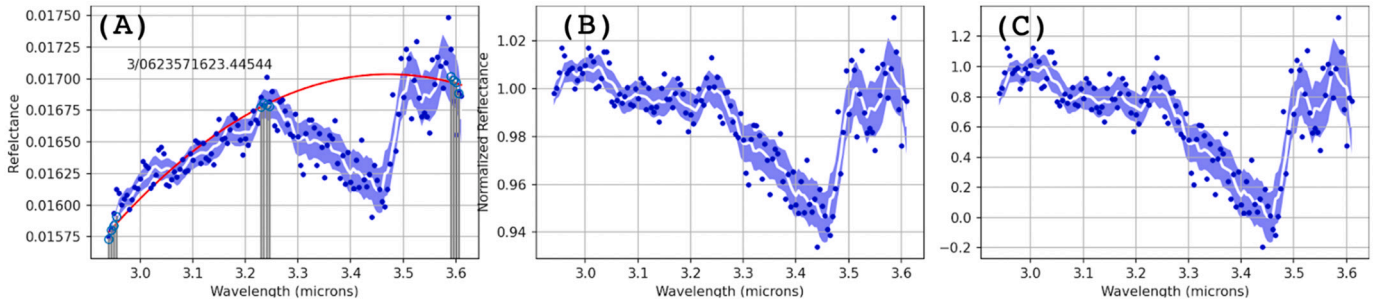

Fig. 2. Blue circles are spectra data points. The left panel **(A)** shows a smoothed OVIRS spectrum (shown as a white line within a purple uncertainty envelope) with spacecraft clock time as an identifier, overlaid with a second-order polynomial fit to the continuum between 3.0 and 3.6 μm (shown in red). Blue dots show the unsmoothed spectral data. The grey vertical lines point to the data points that were used to constrain the polynomial. The center panel **(B)** shows the results of dividing the data by the polynomial (i.e. removing the continuum). The right panel **(C)** shows the spectrum with the absorption band stretched between 0.0 and 1.0, from the band center to the continuum. (For interpretation of the references to colour in this figure legend, the reader is referred to the web version of this article.)

percent carbonate was enough to produce a 3.4-μm band in a mixture of pure mineral endmembers. However, while it only takes a small amount of carbonate to impart an absorption at 3.4 μm, it takes a greater abundance of organics to impart an equivalent 3.4-μm band. The organics band is weak in carbonaceous chondrite meteorites, probably because meteorite organics have low abundances of aliphatic C—H bonds (Donaldson Hanna et al., 2019; Kaplan et al., 2019).

We apply a Kolmogorov-Smirnov similarity test to OVIRS spectral observations of Bennu and laboratory spectra of minerals to categorize 3.4-μm features as attributable to either carbonates (calcite, dolomite, magnesite) or organics (meteoritic aliphatic hydrocarbons, asphaltite, graphite). For this study, we force a choice of one or the other and do not account for ambiguous detections, or the possibility that both carbonates and organics are detected in the same spectrum. (In future work, we will consider the possibility of mixtures of carbonates and organics. Here we are suggesting which phase dominates.) We use carbonate, organic, and insoluble organic material spectra from Kaplan et al. (2019), as well as additional spectra from the NASA RELAB archive (Pieters and Hiroi, 2004).

2. Data set

OVIRS spectra obtained at incidence and/or emission angles greater than 70 degrees were eliminated from the dataset because of poor data quality and consequent difficulty in fitting the photometric disk function . The remaining observations were photometrically corrected using a McEwen (1991) model whose parameters were constrained with spectra obtained during the global survey at a phase angle range of 7 to 130 degrees following Zou et al. (2021) . Spectra are corrected to radiance factor units (I/F) with viewing geometry as follows: incidence angle = 30 degrees, emission angle = 0, and phase angle = 30 degrees. The perimeters of the OVIRS footprints are found by using SPICE kernels (Acton, 1996) and intersecting the OVIRS boresight vector with a global shape model of the asteroid — specifically, the stereophotoclinometric (SPC) v42 shape model (with mean facet edge length 0.8 m) available at http://sbmt.jhuapl.edu (Barnouin et al., 2020; Simon et al., 2020a).

The laboratory spectra were originally obtained from the Reflectance Experiment Laboratory (RELAB, Brown University), the Jet Propulsion Laboratory, Ecospeclib, and the United States Geological Survey (USGS spectral library version 7). The 14 organic matter spectra we use are listed and described in Kaplan et al. (2019), and the carbonate mineral spectra (44 calcites, 25 dolomites, and 15 magnesites) are listed and described in Table S3 of Kaplan et al. (2020a). We list all laboratory spectra in Appendix 1.

Analyses and calculations were performed using MatLab and Python libraries entitled NumPy, Matplotlib, AstroPy, and GeoPandas (MATLAB, 2010; Van der Walt et al., 2011; Hunter, 2007; Robitaille et al., 2013; Price-Whelan et al., 2018; McKinney et al., 2010). The data we used for this analysis (both input laboratory data and output spectral matches) are available in Ferrone et al. (2021b).

The MapCam medium-field imager acquired data during Recon A from altitudes ranging between 1.14 and 1.20 km, resulting in an average pixel scale of 6 cm/pixel (Lauretta et al., 2017, 2021; Rizk et al., 2018). The images were processed with a dark subtraction, charge smear correction, and a flat field normalization, then photometrically corrected to radiance factor (RADF) (with viewing geometry of incidence angle = 30 degrees, emission angle = 0, and phase angle = 30 degrees) using the ROLO (RObotic Lunar Observatory) photometric model as described in Golish et al. (2021). The latitude and longitude coordinates were determined using the Integrated Software for Imagers and Spectrometers (ISIS3). This software made it possible to register pixel coordinates to the v42 shape model of Bennu (Barnouin et al., 2020). Kaplan et al. (2020a) used imaging data obtained by PolyCam, the narrow-angle camera of the OCAMS suite, which has a spatial resolution approximately 5 times that of the MapCam image data. We chose to use the MapCam data instead (where applicable) because these have been controlled and registered to the shape model at the 6 cm/pixel scale (Table 1) (Rizos et al., 2021). For our purposes, the need for accurate pointing for the spectral data was more important than the spatial resolution of the associated images. At the time of this writing, the OVIRS pointing is accurate to within 1.5 m, or roughly 15–35% of a typical OVIRS footprint during the Recon A mission phase.

3. Methods

A full discussion of the calibration of OVIRS measurements to radiance units is provided in Simon et al. (2018). Processing and conversion of the data from radiance to radiance factor includes removal of thermal contamination, as discussed at length in the Appendix of Simon et al. (2020a). Here, we summarize briefly: the thermal tail is removed from each spectrum using a single blackbody fit with emissivity scaling and a fixed spectral slope. To find the thermal radiance for each spectrum, a linear continuum is fitted from 1 to 4 μm, multiplied by a range-corrected solar spectrum, and scaled to Bennu's radiance at ~2.1 μm. This scaled solar radiance is subtracted from the OVIRS spectrum to find the remaining thermal radiance. The thermal radiance spectrum is then fitted with a single temperature blackbody curve, and then scaled to the measured thermal radiance, while minimizing the χ^2 goodness of fit.

After obtaining the preprocessed data, we then process all 15,585 OVIRS spectra collected during reconnaissance A for our purposes by (a) smoothing with a boxcar filter set to a length of nine OVIRS channels, (b) fitting and removing a continuum, and (c) stretching the measured absorption band between 3.2 and 3.6 μm to range from 0.0 and 1.0 (band center is set to 0.0, and continuum is set to 1.0). The uncertainty in the OVIRS spectrum includes absolute radiometric uncertainty and calibration error (Simon et al., 2018). The uncertainties of the OVIRS

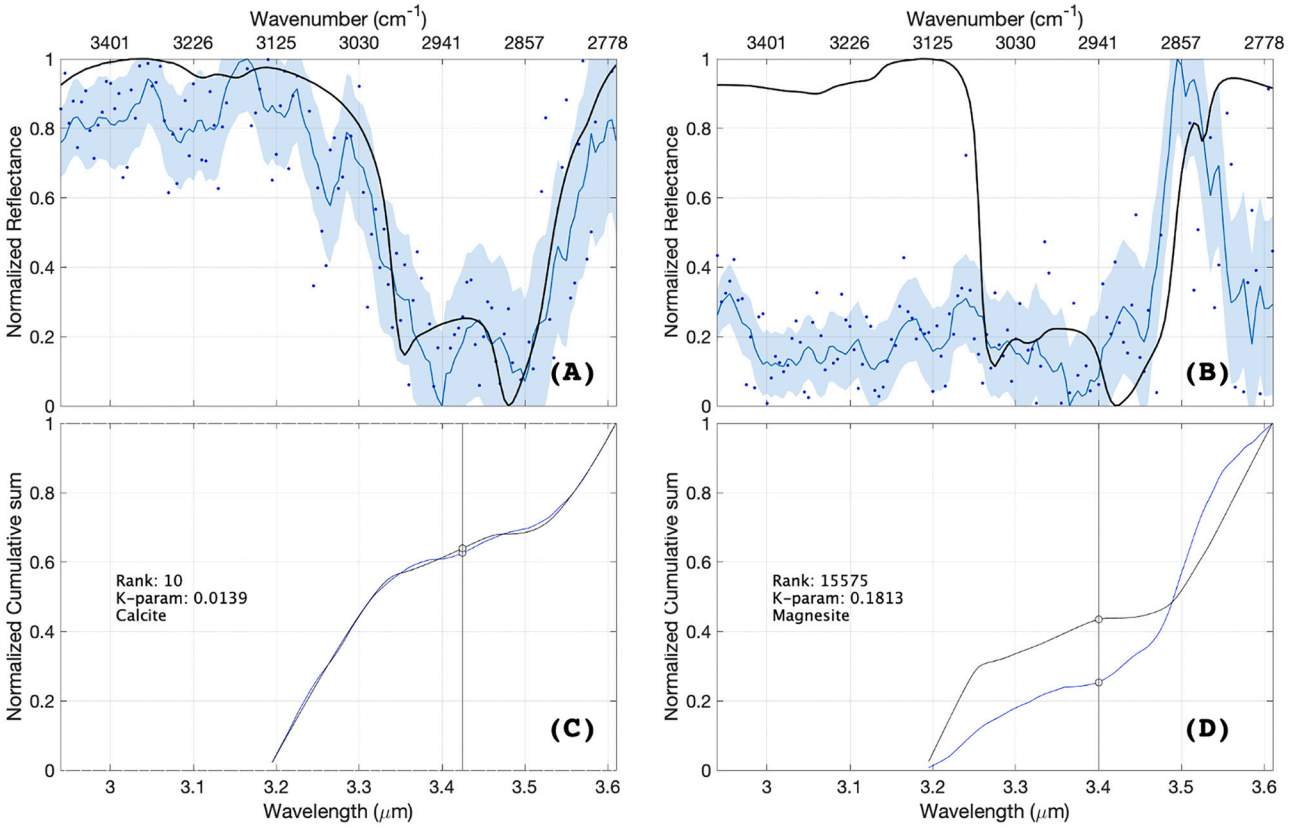

Fig. 3. **(A)** An example of a good match between an OVIRS observation, in blue, obtained from Bennu (on 2019-10-05 at site Sandpiper) and a laboratory spectrum, shown in black, of ALH83100 organic matter. **(B)** An example of a poor match. **(C & D)** The corresponding cumulative distribution functions of the OVIRS spectrum and the laboratory spectrum for panels **A** & **B** respectively, normalized to unity. The vertical lines pinpoint the largest discrepancy between the distributions in wavelength space, this vertical distance is also known as the k-parameter. **A** and **C** correspond to the tenth best match in the data set, while **B** and **D** correspond to the tenth worst match in the data set. (For interpretation of the references to colour in this figure legend, the reader is referred to the web version of this article.)

photometric correction adds a limited degree of uncertainty as discussed in Zou et al. (2021). The boxcar filter is applied over nine adjacent wavelength channels. The errors of each wave-channel are square root summed and divided by the total number of channels within the box. Fig. 2 demonstrates the results of these steps. We perform these steps on all OVIRS observations. In the case of the laboratory data we follow the same procedure for continuum removal yet we do not apply a box car smoothing because the signal-to-noise ratio is sufficient.

After each OVIRS spectrum is prepared, we perform a spectral similarity test against each of the 98 laboratory spectra. We use an adaptation of the Kolmogorov-Smirnov goodness-of-fit test to compare OVIRS and laboratory spectra (Paclik and Duin, 2003). This test is described below and it is useful because it is sensitive to the differences in the shapes of the absorption bands being compared. This method is sensitive enough that it captures small details such as local minima within the wavelengths of comparison. However, in using this method, we do not use data outside of the 3.2- to 3.6-μm region of the spectrum for matching.

The Kolmogorov-Smirnov goodness-of-fit test is designed to compare empirical distributions that have probability density functions that sum to 1 when integrated. The steps of this test are illustrated in Fig. 3. First, we calculate the cumulative sum of the distribution values for each spectrum, as a function of wavelength, between 3.2 and 3.6 μm. We do this by replacing the normalized reflectance value at each discrete OVIRS channel by the sum of reflectance values starting at 3.2 μm. We then normalize each sum to 1.0 at the maximum value. Then we find the maximum discrepancy between the laboratory and OVIRS cumulative sum spectra, i.e., the k-parameter, a measure of goodness of fit. The smaller the k-parameter, the better the spectral match between OVIRS and laboratory measurements. Fig. 3A shows a high-quality fit, whereas Fig. 3B shows a low-quality fit. Spectra are ranked according to the magnitude of the k-parameter, such that rank = 1 is the closest match of an OVIRS spectrum to a laboratory spectrum. The OVIRS spectrum is then classified as either carbonate or organic based on the best match. The laboratory spectrum that has the lowest k-parameter value when tested against an OVIRS spectrum is considered to be the match for that OVIRS spectrum. The OVIRS spectrum in Fig. 3B has no band between 3.2 and 3.6 μm; therefore the suggested "match" is meaningless and nonphysical.

After testing, ranking, and categorizing all OVIRS spectra in our collection, we record a few other characteristics of the data. For each spectrum, we calculate the band depth of the 3.4-μm carbon-species feature (organic or carbonate) and the 2.7-μm hydration feature, the band minimum position (measured as a wavelength) of these features, and spectral slope across two spectral regions (Kaplan et al., 2020a, 2020b). To measure the spectral slopes, we fit first-order polynomials to the reflectance spectra for each of two wavelengths: 0.4 to 0.7 μm (visible slope) and 1.0 to 2.5 μm (infrared slope). For the 3.4-μm absorption feature, we measure the depth of the band after continuum removal as a vertical distance from 1.0 to the minimum value in the spectrum as in Kaplan et al. (2020b). The wavelength of the minimum value is taken as the band minimum position. For the hydration band, we use a linear continuum, constraining the line fit with the reflectance values near 2.5 and 3.7 μm. At each point we use four adjacent channels to fit the continuum line with a linear least squares. After removing the continuum of the hydration band, we follow the same procedure for the band at 2.7 μm as we used for the 3.4-μm feature. Example plots are shown in Ferrone et al. (2021b).

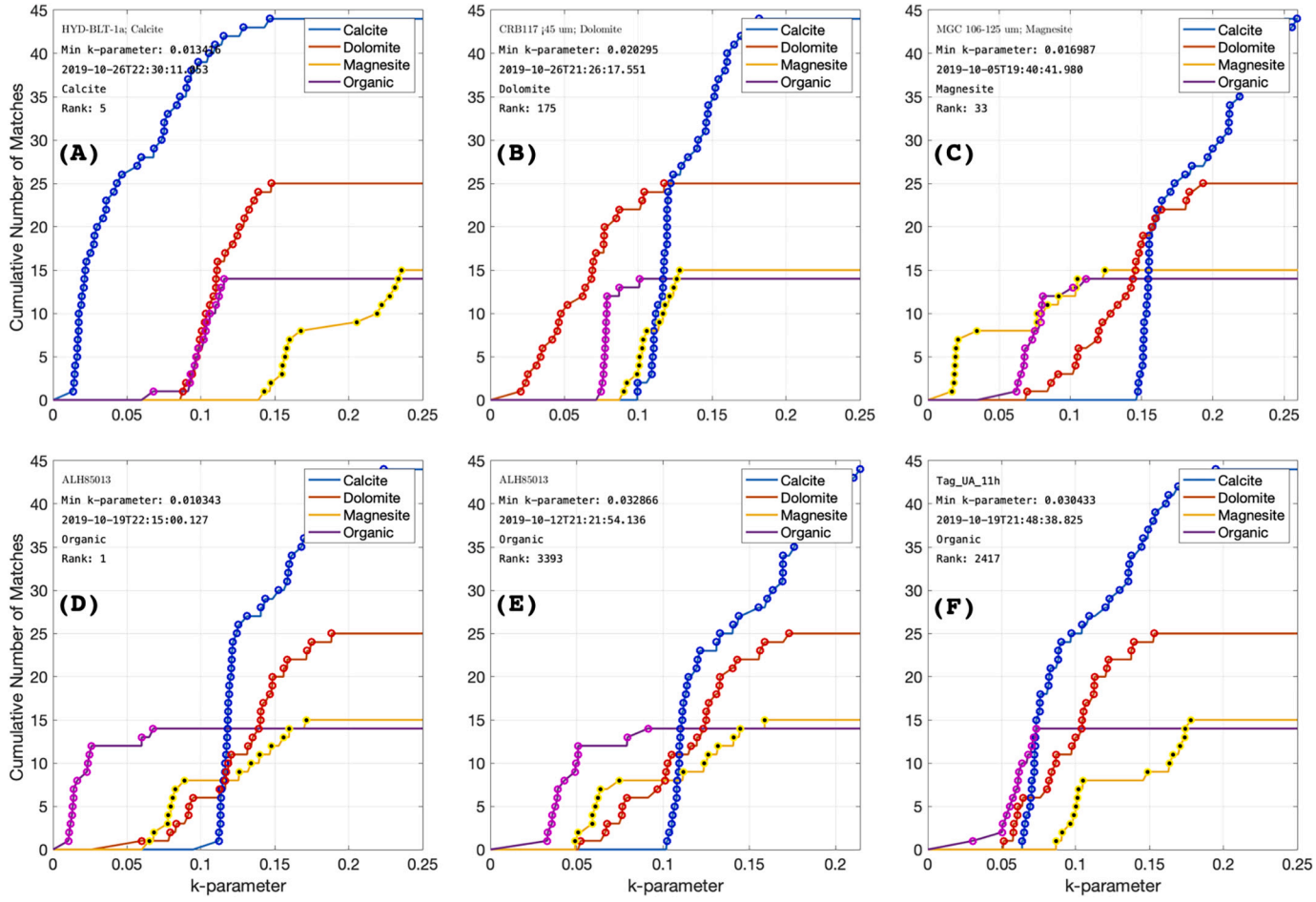

Fig. 4. The cumulative number of times an input spectrum would be identified as carbonate or organic, as a function of k-parameter. A lower k-parameter value indicates a better-quality fit. The more separated each endmember curve is from the others, the less ambiguous the identification for that spectrum. The point markers identify a new match of a laboratory spectrum to an OVIRS spectrum, where each plot is a different OVIRS spectrum as indicated by the timestamp identifier. The text on each plot indicates the name of the best-fitting laboratory sample, the minimum k-parameter value, the date and time of the OVIRS observation, the classification (organic or carbonate) of the OVIRS spectrum, and the rank of the best fit in the data set. We provide an example of each of the following cases, for comparison: **(A)** consistent calcite match (meaning that 27 calcite matches are made before a single organics match is made); **(B)** consistent dolomite match; **(C)** consistent magnesite match; **(D)** consistent organic match; **(E)** weak yet consistent organic match given that the lowest k-parameter value is high (~0.04); **(F)** an initial organic match but ambiguous thereafter because the subsequent matches are dolomites and organics at a much higher k-parameter value than the first match.

In addition to studying the properties of each OVIRS spectrum, we also characterize the MapCam imaging data corresponding to the visible scenes for the OVIRS footprints ranked in the top 5% for goodness of fit with laboratory spectra. These are the detections for which we hold the highest confidence. We also present a case study for site Osprey, where we compare the spatial distributions for the top 5%, top 15%, and top 50% carbonate and organics classifications. We chose Osprey for this case study because it has a ~ 10-m-diameter north-south–oriented bright boulder, called Strix Saxum (see the Gazzeteer of Planetary Nomenclature, n.d). Given its contrast to the surroundings, we wanted to test whether Strix Saxum shows any differences in organics or carbonate signals.

4. Results

4.1. Spectral matching

Our method finds high-quality matches between OVIRS data and laboratory spectra of both carbonates and organics (Figs. 3 and 4 and 5). To gauge the robustness of spectrally matching the laboratory data to the OVIRS data, we test the consistency of example matches. In Fig. 4A, we show that 27 consecutive calcites are matched with an OVIRS spectrum before an organics spectrum is matched. In Fig. 4D, we show that 12 organics are best-matched with an OVIRS spectrum before a dolomite spectrum has the next lowest k-parameter. Fig. 4D also corresponds to the spectrum shown in Fig. 5A. In terms of Fig. 4, the more separated each endmember curve is from the others, the less ambiguous the identification, and vice versa. In Fig. 4A, the calcite is a strongly preferred identification, whereas the dolomite and organics matches are roughly the same quality as each other, and both are far below the calcite match.

With this illustration, we see that the strength of the identification depends on the number of library spectra within each mineral class. We have 14 organic, 15 magnesite, 25 dolomite, and 44 calcite laboratory spectra. Therefore, it is important to consider the irregular sampling of our spectral library in determining the strength of any single detection. Despite having the smallest number of laboratory endmembers, the highest-quality fits tend to be with the organics (see Discussion). For example, the lowest k-parameter value for an organic fit is 0.0103, whereas the lowest k-parameter for a carbonate fit is 0.0134 (see Fig. 5). We show 16 examples of our matching results in Fig. 5, where the top two rows display some of the best matches in the data set, and the bottom two rows show matches for which we have less confidence (k = 0.025 to 0.04).

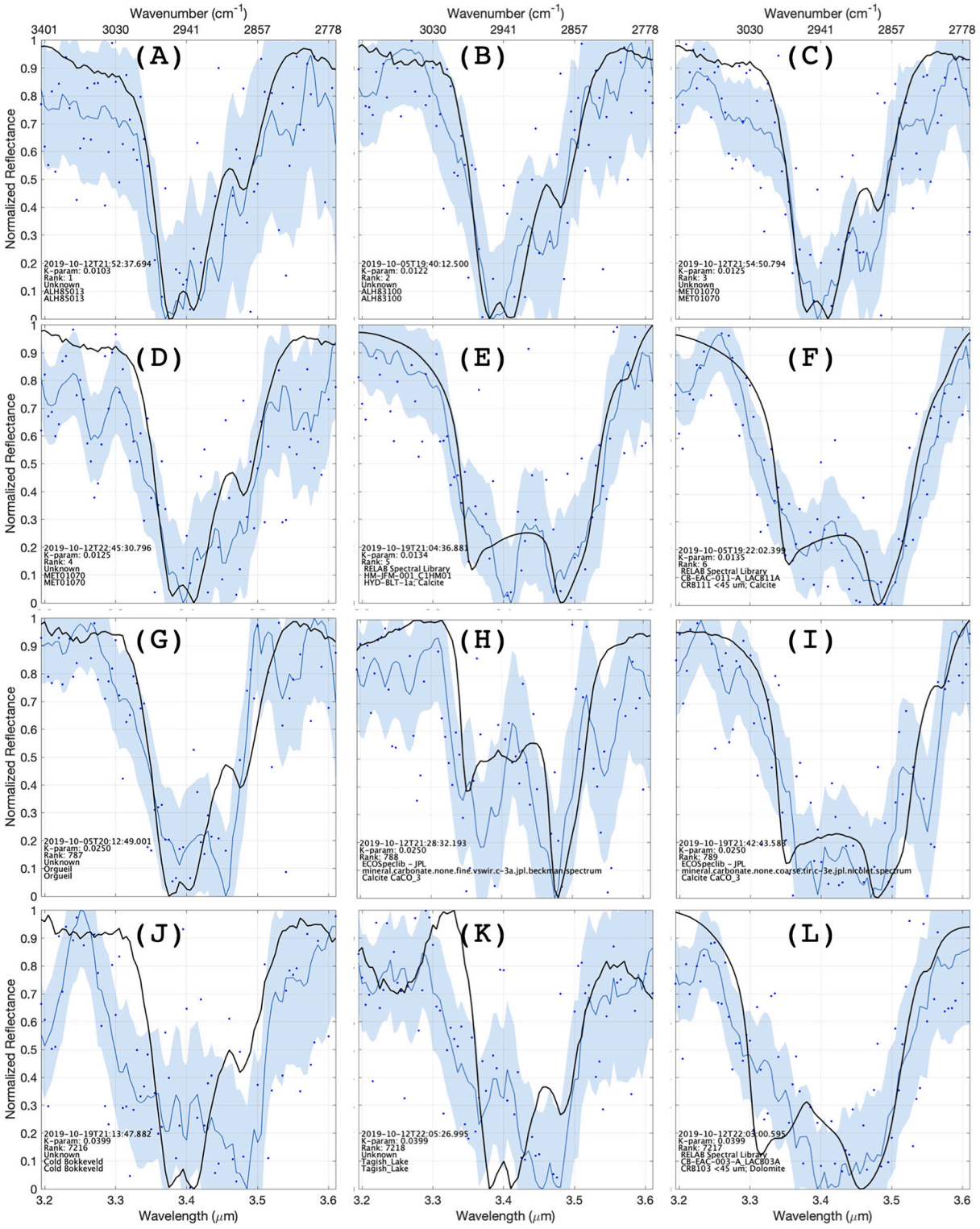

Fig. 5. The range of spectral matches found between laboratory spectra (shown in black) and the OVIRS spectra (shown in blue). Spectra are identified by name in the legends shown at the bottom left of each panel. The top two rows show the best six matches; the third row shows the lower end of the match threshold with k-parameter values just below 0.025; and the bottom row shows matches with k-parameters between 0.025 and 0.04. We consider these last matches to be lower-quality than the best matches but superior to the worst (non-detections) exemplified by Fig. 3b. (For interpretation of the references to colour in this figure legend, the reader is referred to the web version of this article.)

The k-parameter appears to be reliable as a goodness-of-fit metric for matching laboratory data to the OVIRS data. The test accounts for band width, band minimum position, and the doublet shape associated with the carbonate spectra and the shoulder associated with the organic spectra. For example in Fig. 5 panels (C) and (D), the OVIRS spectrum has a long-wavelength shoulder that dips low and appears to be similar to the doublet shape associated with carbonates; however, this feature is narrower in width than carbonate features, therefore it is more closely

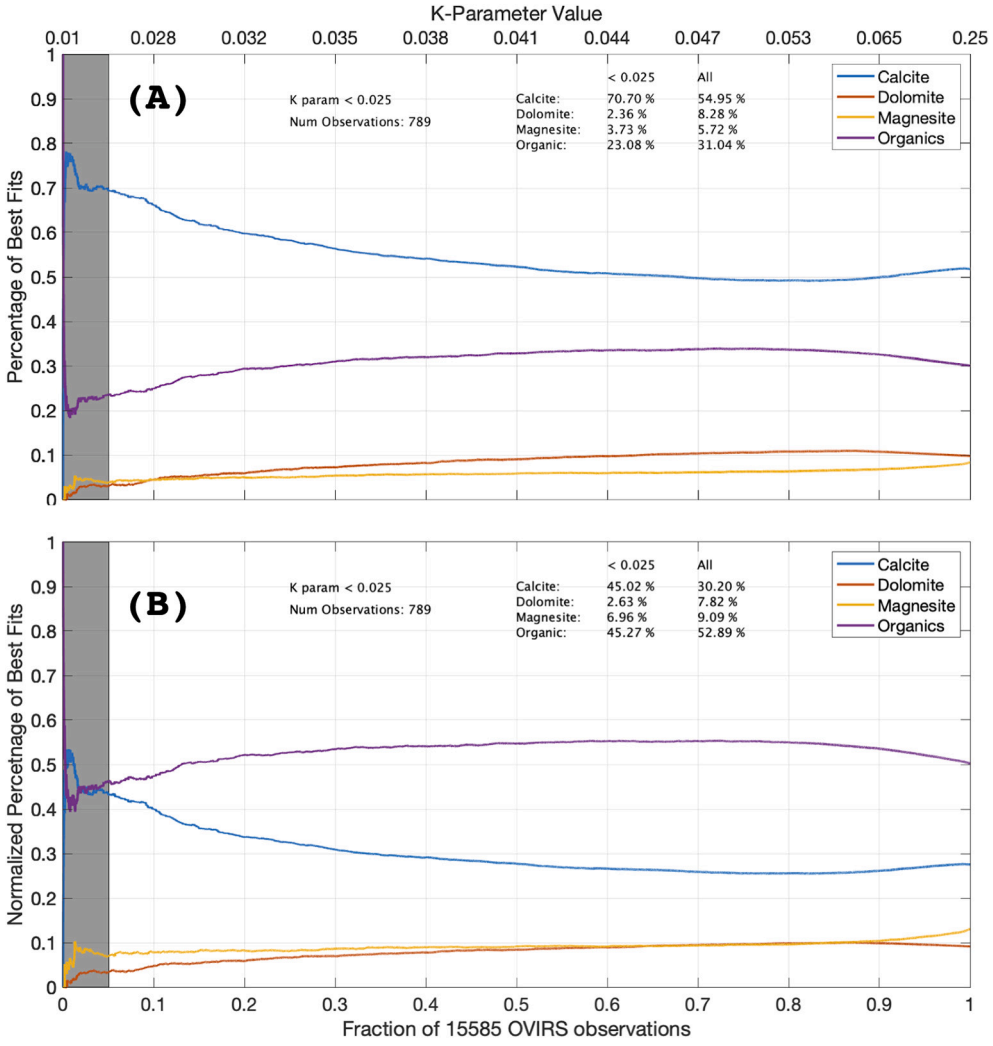

Fig. 6. (**A**) The distribution of matches as a function of the ranked best fit and as a function of the fraction of the total 15,585 spectra. For example, at $x = 0.05$ (top 5% of the dataset; 789 spectra with k-parameter <0.025), 70% of the best matches are calcite, 23% are organics, 5% are dolomite, and 5% are magnesite. The shaded region at the left indicates the top 5%. (**B**) Each curve normalized to the different number of spectra tested per mineral group (44 calcites, 25 dolomites, 15 magnesites, and 14 organic). We integrate under each curve to calculate the total relative proportions, as listed in the legend.

associated with the organics. The spectra of panels (E), (F), (H), and (I) demonstrate the doublet shape associated with carbonates.

After examination of Figs. 4 and 5, we defined our highest-confidence carbonate and organic detections as falling within the top 5% of the OVIRS–laboratory spectral matches (789 out of 15,585 spectral matches with k-parameter <0.025). Fig. 5 illustrates how we set this threshold. The third row of Fig. 5 shows examples of spectral tests that represent the lower limit of quality (but are still within the top 5% of matches). After the third row, the spectral matches do not align well with the laboratory data. Beyond the top 5% (789 spectra with k-parameter <0.025), the fits are ambiguous. That is, the OVIRS data may represent mixtures of carbonate and organics, or may be too noisy to categorize. We refer to the top 5% as the best matches. Henceforth, we use only the OVIRS observations that are better (have a lower k-parameter) than this limit.

It is important to interpret the numerical value of the k-parameter from one fit to another. For instance, the difference between the k-parameter values of the first and second best fits of the data set is 0.002, which is larger than the difference between the second and third (0.0003). This gives us confidence that the very best fit is better than the second. Beyond setting our threshold at 5%, we consider only the rank of each spectral match and do not make quantitative statements of how much better one fit is than another. That is, if the rank of the k-parameter match is within the top 5% of the data set, then we trust our detection as a carbonate or as an organic. If not, we cannot reliably differentiate between them.

Table 2
The differences in distribution of organic-like spectra versus carbonate-like spectra across the main regions of interest. These values are calculated by integrating the distribution of fits as a function of the fraction of the total data as shown in Fig. 6. (k-parameter <0.025) integrates under the shaded area, while (all) integrates over all observations. Num indicates the number of observations.

(k param <0.025)	Calcite	Dolomite	Magnesite	Organic	Num
Sandpiper	82.0%	2.1%	3.0%	12.1%	100
Osprey	61.0%	2.4%	4.8%	31.6%	200
Kingfisher	79.4%	2.9%	2.5%	14.7%	164
Nightingale	60.0%	3.1%	4.5%	31.4%	97
Minokawa Crater	42.8%	1.6%	12.0%	40.3%	33
All Recon A	70.7%	2.4%	3.8%	23.1%	789
(all)	Calcite	Dolomite	Magnesite	Organic	Num
Sandpiper	57.3%	9.3%	5.4%	28.0%	1790
Osprey	53.8%	7.6%	5.6%	33.0%	3713
Kingfisher	60.1%	7.7%	3.7%	28.5%	3170
Nightingale	47.7%	9.8%	8.1%	34.4%	2169
Minokawa Crater	43.5%	9.1%	8.6%	38.8%	647
All Recon A	55.0%	8.3%	5.7%	31.0%	15,585

To gauge the relative distribution of the organics and carbonates on the surface, we plot the fraction of carbonate-like and organic-like spectra as a function of the ranked best fit, shown in Fig. 6. Calcites represent between 50 and 78% of the best matches, whereas organics represent 20 to 35% of the best matches. When all 15,585 spectra are

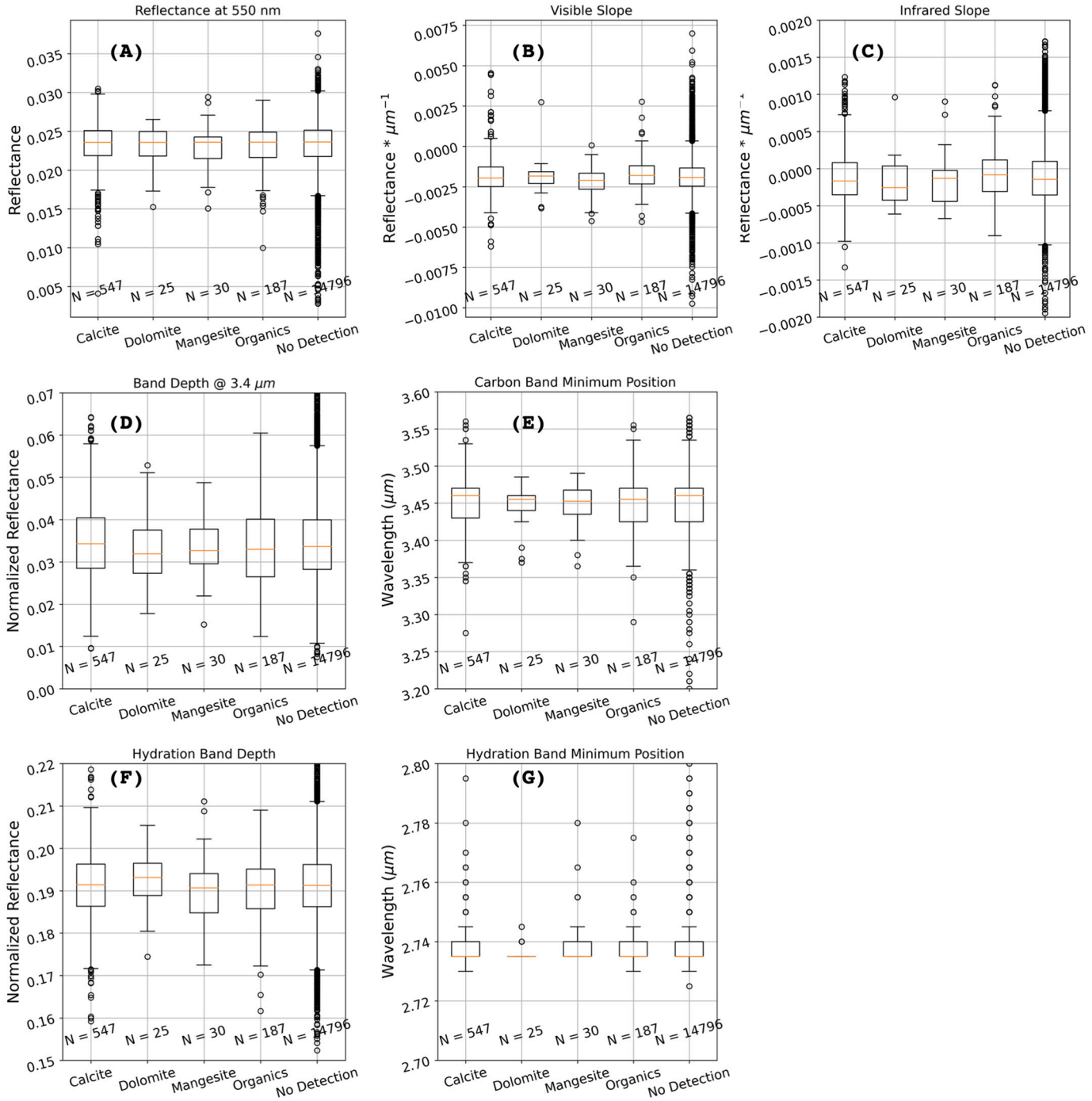

Fig. 7. Box-and-whisker plots of the VIS-IR spectral properties of our top 5% (789 spectra with k-parameters less than 0.025) of organic and carbonate matches. The box width spans the first and third quartile of each data set. The orange line shows the median value. The whisker lengths are 1.5 times the length of the range between the third and fourth quartile. The white circles are data points beyond this range. The boxes in (G) are oddly shaped because the OVIRS channels are quantized into channels of 5 nm. We find no statistical differences in spectral properties between the groups of calcite, dolomite, magnesite, and organics.

categorized, 77% of observations are more carbonate-like and 23% are organic-like. We report these values in Table 2.

To further examine the effect of our spectral library containing different numbers of spectra for different minerals, we perform a secondary check by calculating the weighted distribution of mineral abundances accounting for the unequal number of spectral samples per mineral. We do this by normalizing each mineral distribution curve from Fig. 6a by the number of samples per mineral. For example, we divide each of the calcite abundance values of Fig. 6a by 44, the number of calcite samples. We do this for each mineral, as shown in Fig. 6b. In the normalized plot, if spectral matching occurred randomly, we would expect calcites, dolomites, magnesites, and organics to be evenly distributed each at 25%. Instead, we find the distribution for all observations with $k < 0.025$ to be [45, 3, 7, 45] %, respectively. This suggests that finding more frequent matches to calcites than organics is a statistically meaningful result, and not simply an artifact of having more calcite endmembers in our spectral library. What is more, applying this normalized statistic would be valid if and only if matching between OVIRS and laboratory spectra occurred randomly. Since this is not the case, as shown in Fig. 4, this establishes the lower and upper bounds of

Table 3
Average values from OVIRS data obtained during Recon A passes over each region of interest. Errors are one standard deviation from the mean for each measurement. BMP is the band minimum position in microns, BD is band depth expressed as a fraction from the continuum. REFF is reflectance factor. *Indicates the average of the entire region shown in Fig. 1 (not restricted to the named site or crater at the center).

	REFF @ 550 nm	Visible slope (1/μm)	Infrared slope (1/μm)	3.4 μm band depth (Δ reff)	3.4 μm band minimum position (μm)	2.7 μm band depth (Δ reff)	2.7 μm band minimum position (μm)
Sandpiper*	0.023 ± 0.003	−0.002 ± 0.001	−0.0001 ± 0.0004	0.035 ± 0.01	3.45 ± 0.04	0.19 ± 0.01	2.74 ± 0.03
Osprey*	0.023 ± 0.003	−0.002 ± 0.00	−0.0001 ± 0.0004	0.035 ± 0.01	3.45 ± 0.04	0.191 ± 0.009	2.74 ± 0.02
Kingfisher*	0.023 ± 0.003	−0.002 ± 0.001	−0.0001 ± 0.0004	0.035 ± 0.01	3.45 ± 0.04	0.191 ± 0.009	2.738 ± 0.007
Nightingale*	0.023 ± 0.003	−0.002 ± 0.001	−0.0001 ± 0.0004	0.034 ± 0.01	3.45 ± 0.04	0.191 ± 0.008	2.739 ± 0.007
Minokawa Crater (#6 in Deshapriya et al., 2021)*	0.023 ± 0.003	-0.002 ± 0.001	-0.0001 ± 0.0004	0.035 ± 0.01	3.45 ± 0.04	0.191 ± 0.009	2.74 ± 0.03

the frequency of matches. I.e. the lower bound of calcite matches being roughly 45.0% while for organics the upper bound being, coincidentally, 45%.

We also examine what happens when we bin the best matches according to their location (Table 2). We find more organics-matching observations from the Nightingale, Osprey, and Minokawa Crater areas than the two other locations observed during Recon A, Kingfisher and Sandpiper. Conversely, we find that Kingfisher and Sandpiper have more carbonate-matching observations. The observed regions extend beyond the boundaries of the candidate sample sites and include all OVIRS observations within the observation sequence as shown in Fig. 1.

To examine the relationship between carbon species and OVIRS spectral parameters, we show the visible slope, infrared slope, band depth and band minimum position of the 3.4-μm and 2.7-μm hydration bands, and the albedo at 550 nm for only the best-matched 789 spectra (top 5%) with k-parameter values below 0.025. (Fig. 7). We find no statistical relationship between carbon species and these spectral parameters. The frequency of values for dolomite-like and magnesite-like spectra differ from the organic-like, carbonate-like, and non-matched spectra. We attribute this to the small number of data points used to constrain the distribution (N = 25 for dolomite and N = 30 for magnesite). The carbonates and organics have the same general distribution as the global distribution, namely, single-peak and skewed distributions. For example, albedo skews toward darkening and slope skews toward reddening (Barucci et al., 2020).

In Table 3 we show the average spectral parameter values for each location observed in Recon A. These statistics include regional data around the named sites shown in Fig. 1. We find that the slope, albedo, and band minimum positions of the 3.4- and 2.7-μm bands do not significantly differ from site to site. We made this table to search for correlations between organic/carbonate detections and other spectral parameters. As discussed previously, the results in Table 2 demonstrate differences between the regions in frequency of carbonate and organic detections. However, the regional average spectral parameters trend toward the global average. This result is different from that presented by Barucci et al. (2020), who found differences in spectral slope and albedo for each candidate sample site. This is because we include all regional data around each of the sites, whereas Barucci et al. look at only the sites themselves. We chose to examine all the regional data in the Recon A dataset because there are not enough spots in our 5% threshold dataset to make meaningful statistical statements about each individual site.

Throughout our discussion thus far, our approach has been to categorize each OVIRS observation as being carbonate-like or organic-like. Assessing the quality of these associations in terms of k-parameter values, we have said that we are confident in our categorization of at least 789 spectra. That leaves a large number; 13,796 spectra that are more ambiguous, and harder to categorize. However, because both carbonates and organics are ubiquitous on Bennu, the majority of the OVIRS spectra may record mixtures of carbonates and organics. A full analysis of this possibility should examine intimate mixtures of these components, in various proportions, to study the systematics of their occurrence, which is beyond the scope of the present paper. Instead, in Fig. 8 we illustrate a typical example of an OVIRS spectrum (the same OVIRS spectrum as in Fig. 5L, but shown with a different dolomite laboratory spectrum) that was not categorized as either carbonate-like or organic-like, and we show that a simple linear mixture of 65% dolomite and 35% organics, does a credible job of reproducing the major features of a 3.4-μm band observed on Bennu. This suggests that many of

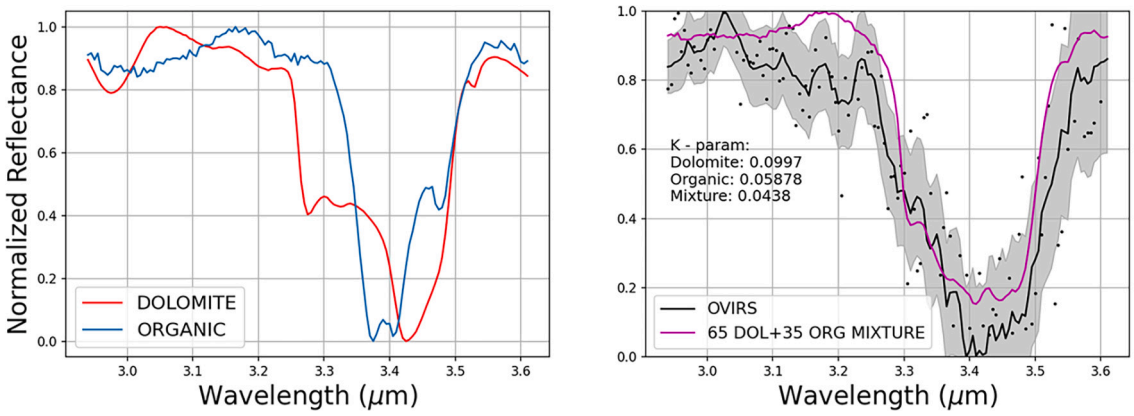

Fig. 8. Normalized and stretched spectra for (left panel) laboratory samples of dolomite and organics and (right panel) a mixture of 65% dolomite and 35% organics, compared with a typical spectrum of Bennu. This example illustrates that a simple linear mixture of carbonates and organics does a credible job of reproducing the major features of a 3.4-μm band observed on Bennu. The Bennu spectrum covers Lon 56.4E Lat 45.5 N, and was obtained on 2019-10-26. The dolomite shown is $CaMg(CO_3)_2$ with filename: mineral.carbonate. None.fine.tir.c-5c.jpl.nicolet. The organic shown is from the C2-ungrouped meteorite Bells.

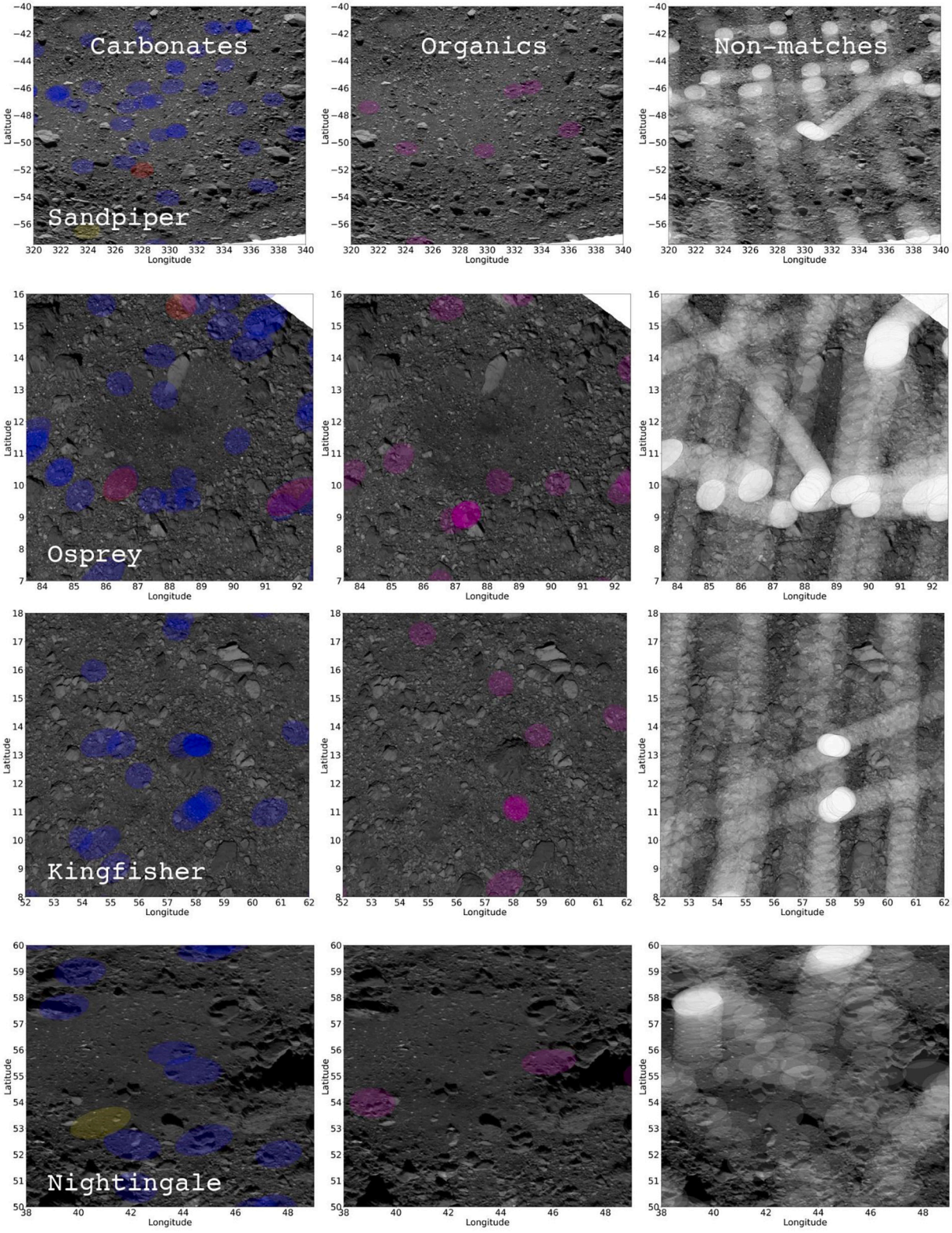

Fig. 9. The first column shows the best matches for carbonates with the k-parameter <0.025 (carbonates), whereas the second shows the matches for organics with the k-parameter <0.025 (organics), and the last column shows spectra that are not identified as either carbonate or organic. The footprint size is determined by the field of view of the spacecraft, not the extent of the detected material. Each row corresponds to a region of interest, from top to bottom: Sandpiper, Osprey, Kingfisher, and Nightingale. Calcites are shown in blue, magnesites in yellow, and dolomites in red (purple when dolomite and calcite detections overlap). Organics are shown in magenta and non-matches in white. Note that overlap of red and blue footprints creates purple in the first column, but these are all carbonates (not organics). (For interpretation of the references to colour in this figure legend, the reader is referred to the web version of this article.)

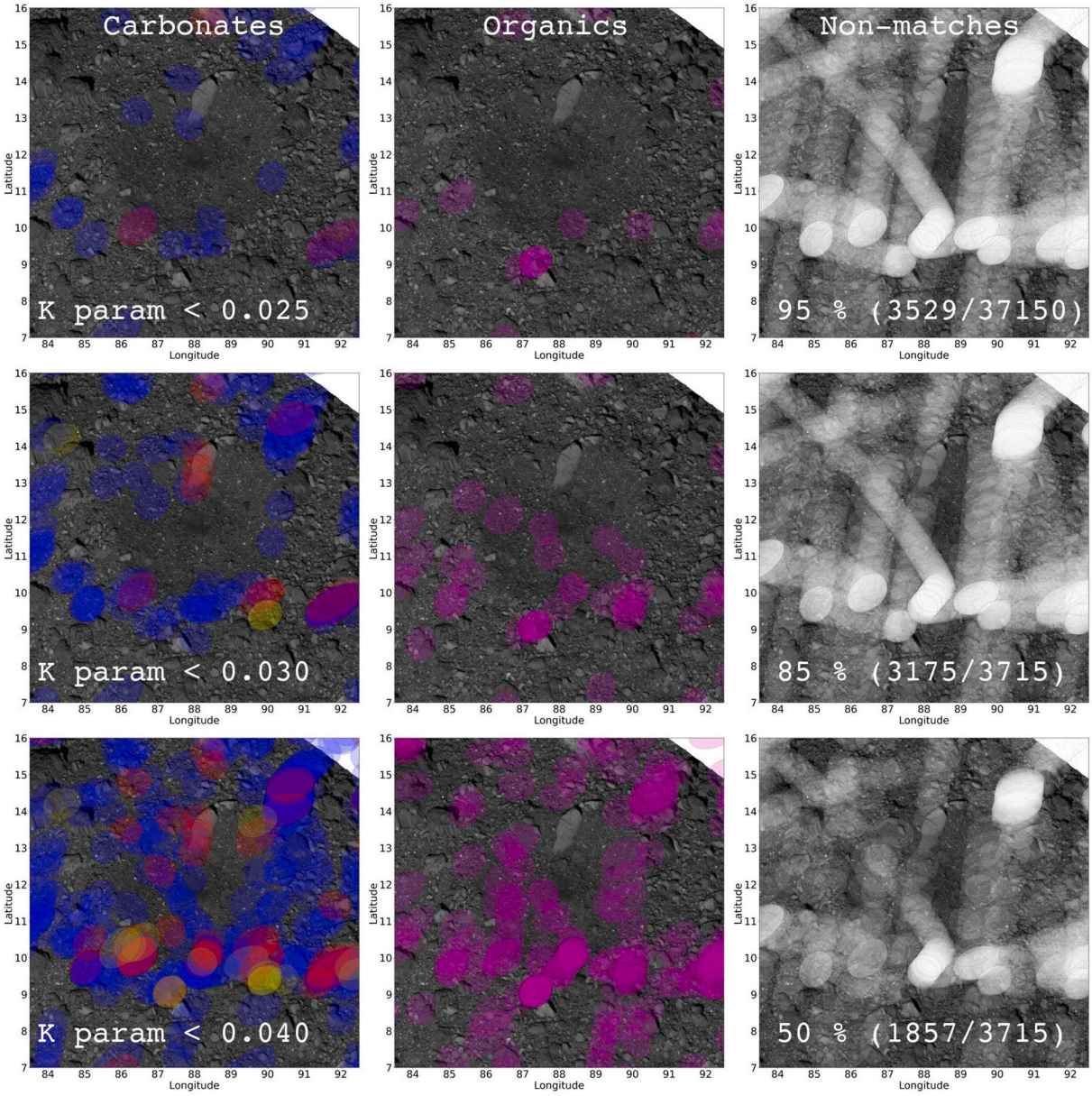

Fig. 10. As in Fig. 9, but for the distributions of carbonates **(left)** and organics **(center)** as a function of k-parameter value for the Osprey site. Non-matches **(right)** are just as frequent as matches. **(Top)** With a threshold k-parameter value at <0.025, 5 to 6% of the dataset meets the criterion and the map is sparsely populated. **(Center)** With a threshold k-parameter value at <0.030, 15% of the dataset meets the criterion. **(Bottom)** Similarly, a k-parameter value of <0.040 results in a map of 50% of the dataset.

the remaining 13,796 spectra in our dataset are likely to be consistent with mixtures of carbonates and organics. A smaller number are too noisy due to low signal to be useful.

5. Characterizing the scenes in each spectral footprint

Here we assess whether our spectral classification groups are associated with surface features or properties independently measured by the MapCam imager. Bennu's surface has craters, an equatorial bulge, small discontinuous regolith-covered regions, and boulders of various sizes (e.g., Walsh et al., 2019). OVIRS spectra best matched by carbonates and those best matched by organics are typically distributed across a site rather than clustered in any given area (Fig. 9).

In Fig. 10 we explore the distribution in and around Osprey of the organic- and carbonate-like spectra as a function of the threshold k-parameter value. We find that increasing the k-parameter threshold increases the numbers of locations showing matches, as expected, but does not reveal any patterns that are clearly related to the surface features visible in the images. Specifically, carbonates and organics are located within and around craters and boulders, showing no obvious preference. There is one possible exception, however: magnesite carbonates are detected on Strix Saxum in many OVIRS spots. This is an intriguing result that may merit follow-up study. Despite this, these matches do not meet our threshold k-parameter, thus while this is an interesting result we are not so confident as to claim that Strix Saxum is especially abundant in carbonates.

The Recon A OVIRS spectra that we analyze here were obtained when the spacecraft was slewing and periodically staring at the same place for the purposes of colour imaging. Fig. 11 shows how the spectra from a single "stare" compare with each other. In the example sequence shown, only the spectrum shown in blue met the threshold requirements we set for identifying the best matches (k-parameter <0.025); however,

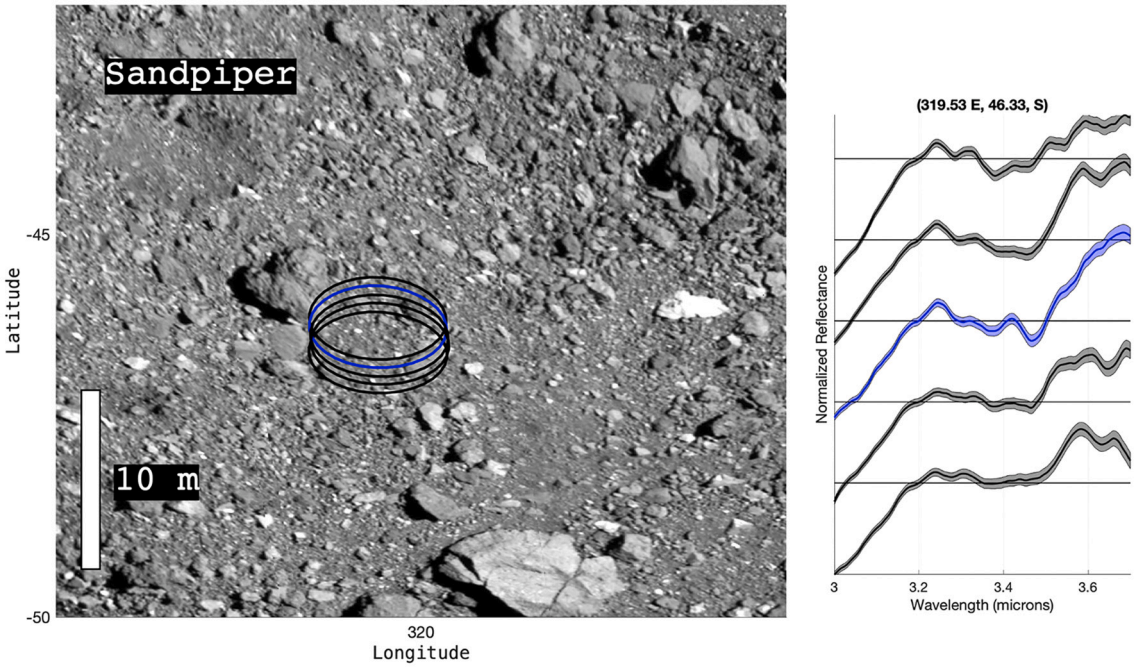

Fig. 11. In this example sequence of OVIRS observations at Sandpiper, only the blue spectrum met the threshold requirement of k-parameter <0.025 for an excellent match. However, the other spectra in the sequence also seem to show the carbonate spectral feature, or a mixture of carbonates and organics, and their k-parameter values are within the range 0.025 to 0.040. (For interpretation of the references to colour in this figure legend, the reader is referred to the web version of this article.)

the other spectra in the sequence (k-parameter between 0.025 and 0.040) also show the carbonate spectral feature. The fact that the band shape for each observation is similar testifies to the reliability of the OVIRS instrument. This demonstrates that setting the detection threshold at a k-parameter <0.025 is a conservative assumption, and detections made above (lower k-parameter) this threshold are reliable.

Because carbonates are known to be bright minerals, as compared with organics, it is reasonable to ask if our best carbonate detections, made spectrally, are associated with brighter materials visible in the MapCam imagery. To answer this question, we seek a statistically meaningful comparison of the brightness of all MapCam pixels in carbonate-detected OVIRS footprints and the brightness of all MapCam pixels in organic-detected OVIRS footprints. Fig. 12 shows values we calculated from the image data within each OVIRS footprint for our top spectral matches. As a basis of comparison, we include data for the spectral footprints for which organic or carbonate detections occur at k-parameter values >0.025. Numerically, there are 15,585–789 = 14,796 spectra with either no detections or weak detections. Very few of these spectra have band depths of zero, so most of these are likely to be mixtures, noisy data, and/or a result of our decision to use a conservative threshold value. Fig. 12 also shows that no statistically significant brightness differences (measured in units of radiance factor at 550 nm) are found between carbonate-detected OVIRS footprints and organic-detected OVIRS footprints. This result could be telling us that, on average, these materials are well mixed below the spatial resolution of the spectrometer footprint, and possibly also below the spatial resolution of the MapCam pixels.

It is also reasonable to ask if the MapCam pixel values we show in the boxes in Fig. 12 are correlated with other properties of their associated OVIRS spectra. For example, are the MapCam pixel values for organics-detected footprints correlated with spectral slope, or band depth at 3.4 μm? In Fig. 13, we investigate whether our three compositional groups—carbonates, organics, and non-detections—show any correlations between spectral properties measured by OVIRS and reflectance properties measured by MapCam. We measured the following spectral quantities from the OVIRS spots: visible slope from 0.4 to 0.7 μm, infrared slope from 1.0 to 2.5 μm, band depth of the 2.7-μm hydration feature, and band depth of the 3.4-μm carbonate/organic feature. We find no statistical relationships between any of these parameters for any of the three compositional groups. Thus, there is no discernable connection between the surface morphological expressions and carbonate or organic grouping at the spatial scales we have sampled (OVIRS, 4 to 9 m/footprint). This supports the finding that the carbonates and organics are ubiquitous across the surface of Bennu at OVIRS spatial scales (Simon et al., 2020a).

6. Discussion

Overall, we find that the Kolomogorov-Smirnov method works well in terms of capturing the shape details of an absorption feature (band width and doublet shape). We suggest that this technique is a viable means of classifying and/or interpreting spectra, particularly for absorption features with compound structure. Our results compare very well with those of Kaplan et al., 2020a for the region of overlap (Nightingale), and we suggest that each study supports the other. Some of the drawbacks of the method that we used are that we do not capture band depth information, and we restrict our analysis to a limited wavelength range, ignoring the overall behavior of the spectrum. The advantages of this method over the linear least squares classification method used in Kaplan et al. are that the Kolomogorov-Smirnov method has greater fidelity to the doublet shapes and overall width of the bands. The linear least squares method treats all data points as equally important and allows the algorithm to smoothly average through the data points, whereas the Kolomogorov-Smirnov method insists on the specific shape of the features and does not allow smoothing.

Because our dataset does not represent complete coverage of the surface of Bennu, we cannot study relative abundances of carbonates vs. organics as a function of location on the surface. We can say that, of the locations observed, calcite-matching spectra are most common.

We have constrained the range of spectral matches given the unequal number of spectra per mineral type in our spectral library by normalizing the number of detections of each mineral type tested by the number of samples of each mineral. If the spectral matching procedure were random, we would expect a ~ 25% detection rate for each of the

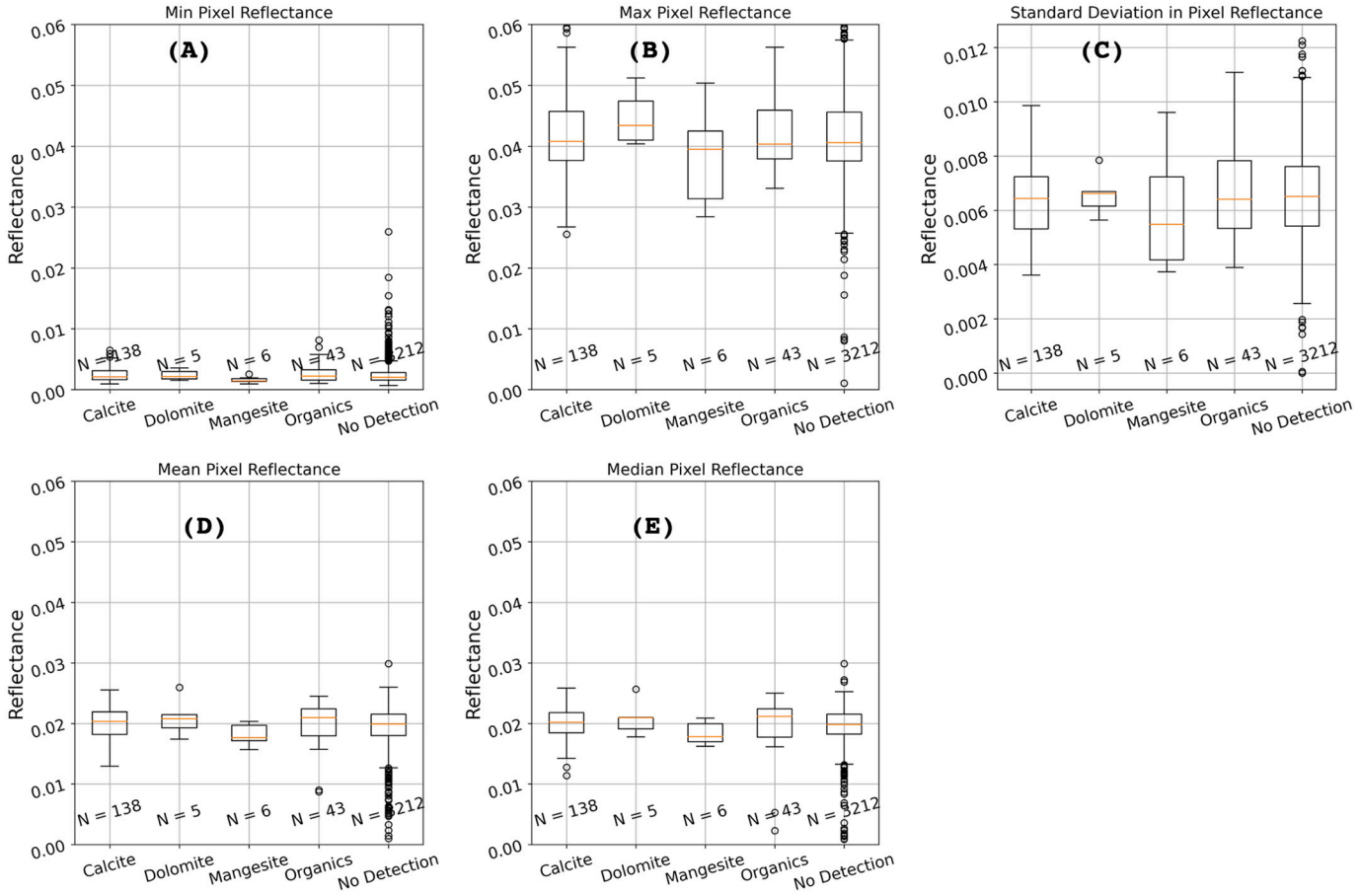

Fig. 12. Distributions of metrics obtained for image data in units of I/F: minimum, median, mean, maximum, and standard deviation of all pixel values within each OVIRS footprint. The magnesite and dolomite distributions appear to be less favored; however, this may be a result of the small number of matches. Calcites, organics, and OVIRS spectra without a detection have similar distributions for each of these quantities. Data are in units of I/F (a.k.a. radiance factor, at 550 nm): minimum, median, mean, maximum, and standard deviation of all pixel values for each of the calcite, dolomite, magnesite, and organic groups.

four mineral types tested. Because we find calcites and organics at a 45% detection rate and dolomites and magnesite at a 5% rate, the spectral matches with Bennu spectra are not random. For example, if an OVIRS spectrum matches a calcite, the next best matches are also calcites. By combining the detection rate of normalized and non-normalized results, we constrain the detection rates of calcites to be 45–70%, while organics are 30–45%, and dolomite and magnesite are 5–10% each. Thus, we conclude the higher rates of detection for calcites and organics are meaningful and representative of the surface of Bennu, whereas dolomites and magnesites are less abundant. This is consistent with other studies that found evidence for aqueous alteration of the surface materials on Bennu (Hamilton et al., 2019; Simon et al., 2020a; Kaplan et al., 2020a; Praet et al., 2020).

We also notice that the highest-quality fits are for organics. A possible reason for this is that the carbonate doublet shapes are smaller than the instrumental noise in this region, whereas the organics have simple and symmetrical band features. This means that the organics features are easier to fit (more likely to have lower k-parameter values), given the random nature of the noise.

We did not investigate other spectral bands on Bennu's surface to search for organics and carbonates. However, Simon et al. (2020b) found that many of the minor bands in the 0.5- to-2.5 μm region are diagnostic of magnesium- and iron-bearing phyllosilicates. As indicated in Simon et al. (2020b), an absorption band observed at 0.55 μm is best attributed to magnetite, which indicates past aqueous alteration. Some carbonate species also exhibit a 3.9-μm absorption feature. We did not include the 3.9- to 4.2-μm region of the OVIRS data in our analysis due to low signal-to-noise ratio. However, in the supplemental materials of Kaplan et al. (2020a), the band depths of the 3.4 and the (more noisy) 3.9-μm band (attributed to calcites) are shown to trend together with an R^2 of 0.4.

According to Kaplan et al. (2020a) and references therein, we should expect to detect more carbonates than organics on Bennu, because even if they started out in equal proportions, in the presence of solar radiation, organic molecules are more prone to break down and disaggregate than carbonate minerals. However, our methods do not allow us to translate the number of detections we find into abundance estimates.

The fact that we do not detect any notable correlations between the carbonate/organic detections and other spectral properties suggests that the factors that control variations in those spectral properties (such as visible-near infrared spectral slope, albedo, and depth of the 2.7-μm band) are independent of the compositional factors that control which species (carbonates or organics) dominate the 3.4-μm band region. This could mean that the spectral slope and albedo variations we observe are sensitive to variations in physical properties on Bennu, such as roughness, texture, grain size, and porosity variations, whereas the 3.4-μm region is sensitive to composition only. Additionally, the OVIRS spot size is too large to spatially resolve organics from carbonates, even though the instrument can detect both phases. Because carbonates and organics are mixed below the spatial resolution of the OVIRS spectrometer, OVIRS is seeing the mixture. (We also know that carbonaceous chondrites have very fine-grained mixtures of these components.) Typically, carbonates have a very high albedo, and organics have a very low albedo. However, while it is true that a few percent of carbon lampblack

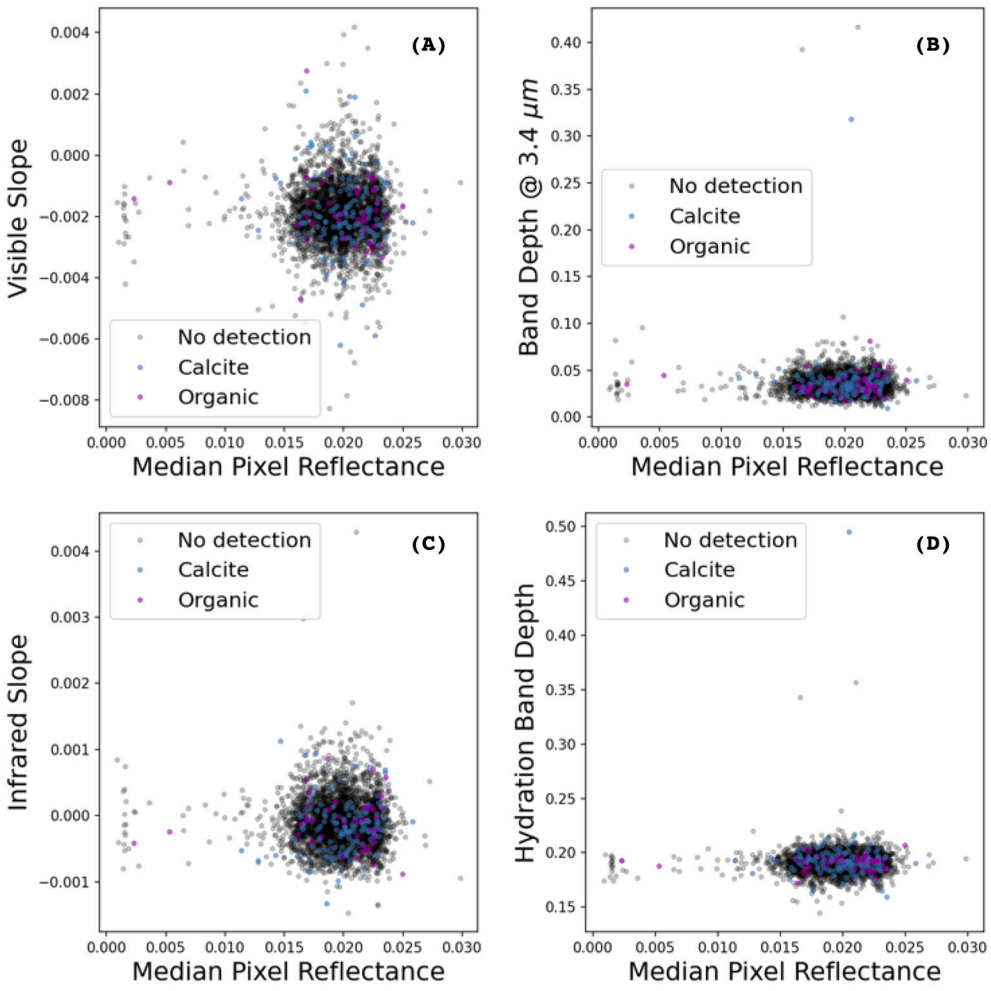

Fig. 13. (A to D) Scatter plots comparing OVIRS spectral quantities (y-axis) with OCAMS (MapCam) reflectance median values at 0.55 μm (x-axis). The x-axis of each plot is the median MapCam pixel value within the FOV of the corresponding OVIRS observation. The y-axes are spectral quantities observed from OVIRS, including the visible slope from 0.4 to 0.7 μm, the infrared slope from 1.0 to 2.5 μm, the band depth of the 2.7-μm hydration feature, and the band depth of the 3.4-μm carbonate/organic feature.

can dramatically reduce the albedo of a substrate, it is not true that a few percent of carbonate can increase the albedo of the same substrate to the same degree.

According to DellaGiustina et al. (2020), boulders are the primary source of heterogeneity on Bennu. While the darker rougher boulders on Bennu appear in size ranges up to 95 m diameter, the brighter and smoother boulders are <10 m in diameter (DellaGiustina et al., 2020). Given the spatial scale of the OVIRS footprint (4 to 9 m in diameter), only boulders larger than this size can fill the OVIRS field of view, and these are relatively rare in the Recon A data because that mission phase targeted the more regolith-rich surface regions on Bennu for the purposes of sample acquisition. This means that most of the OVIRS spots fall on mixtures of smaller rocks of both types, and spots that are fully filled by a single boulder type are rare, making a statistical study beyond our reach. While DellaGiustina et al. (2020) are able to describe the properties of spatially resolved individual boulders at the spatial resolution of MapCam (<30 cm/pixel), such a study with OVIRS data remains elusive. This mismatch between the spatial resolutions of the two instruments (MapCam and OVIRS) is visible in the analyses we show in Figs. 9 to 13. Our OVIRS spots are too large to assess a correlation between carbonate/organic detection and boulder type.

7. Conclusions & future work

Organics and carbonates are found at each of the locations studied on asteroid Bennu during the Recon A phase of the OSIRIS-REx mission, which offered sufficient resolution to distinguish these carbon-bearing species. The carbon-species classifications of spectrometer spots in this dataset do not seem to correlate with quantitative metrics of surface properties measured with either OVIRS or OCAMS. Specifically, we find no statistical associations between organics and spectrally red or dark locations on Bennu. We find no statistical relationship between carbon species and continuum slope, band minimum position, or band depth. This could mean that either (1) carbonates and organics are ubiquitous across the surface or (2) our spectral data do not have sufficiently high spatial resolution to draw meaningful associations between surface features and carbon species (in other words, the connections may occur at spatial scales smaller than 4–9 m). This finding could help to constrain areal mixing studies.

Are the five locations studied distinct with respect to their carbonates and organics? We find that more organic-spectral matches occur in the Nightingale, Osprey, and Minokawa Crater regions than the other locations observed during Recon A. Organic molecules are known to break down in the presence of solar wind (Simon et al., 2020a), perhaps providing a relative age relationship for dating craters on Bennu. Higher concentrations of organics at the Nightingale, Osprey, and Minokawa Crater regions could indicate that these areas were more recently exposed, perhaps by recent crater formation. If this interpretation is correct, then the samples obtained by OSIRIS-REx at Nightingale may be richer in organics than the average Bennu surface.

Seventy percent of the best matches between OVIRS spectra and laboratory measurements are carbonates, and 30% of best matches are organics. Once we account for the different numbers of laboratory spectra that are tested (84 carbonates and 14 organics), this ratio gets closer to 49:51. This means that when we are able to detect a carbon species, carbonates are detected between 49 and 70% of the time, and

organics are detected between 30 and 51% of the time. In other words, our method is more sensitive to carbonates than organics. What this means in terms of relative abundance on Bennu is difficult to say because we have not considered cases where both carbonates and organics may be detected or mixed.

Data availability

OVIRS spectra (Reuter et al., 2019) and MapCam images (Rizk et al., 2019) from Recon A are available via the Planetary Data System. MapCam images used in this work are reported in Table 1. The global SPC shape model v42 is available in the Bennu section of the Small Body Mapping Tool (http://sbmt.jhuapl.edu/). Data from the analyses and calculations are provided in Ferrone et al. (2021b). Spectral data used in this study are available from the following facilities: The ECOSpeclib JPL Facility: https://speclib.jpl.nasa.gov/library; Kaplan et al. (2019); the USGS Spectral Laboratory: https://www.usgs.gov/labs/spec-lab; and the Keck/NASA Reflectance Experiment Laboratory (RELAB) at Brown University: http://www.planetary.brown.edu/relab/. See Appendix 1 for spectra filenames.

Declaration of Competing Interest

None.

Acknowledgments

We are grateful to the entire OSIRIS-REx Team for making the encounter with Bennu possible. This material is based upon work supported by NASA under Contract NNM10AA11C issued through the New Frontiers Program. J.R.B. and G.P. acknowledge support from Italian Space Agency grant agreement no. 2017-37-H.0.

Appendix 1

Mineral	Source	Sample	File name
Calcite	RELAB	CAL110 < 45 um	CA-EAC-010_M1CA10
Calcite	RELAB	CRB109 < 45 um	CB-EAC-009-A_LACB09A
Calcite	RELAB	CRB109 45–90 um	CB-EAC-009-B_LACB09B
Calcite	RELAB	CRB110 < 45 um	CB-EAC-010-A_LACB10A
Calcite	RELAB	CRB111 < 45 um	CB-EAC-011-A_LACB11A
Calcite	RELAB	CRB112 < 45 um	CB-EAC-012-A_LACB12A
Calcite	RELAB	CRB112 45–90 um	CB-EAC-012-B_LACB12B
Manganocalcite	RELAB	CRB113 < 45 um	CB-EAC-013-A_LACB13A
Manganocalcite	RELAB	CRB113 45–90 um	CB-EAC-013-B_LACB13B
Calcite	RELAB	CRB128 < 45 um	CB-EAC-063-A_BKR1CB063A
Calcite	RELAB	CRB130 < 45 um	CB-EAC-064-A_BKR1CB064A
Calcite	RELAB	CRB131 < 45 um	CB-EAC-065-A_BKR1CB065A
Calcite	RELAB	CRB131 < 45 um	CB-EAC-065-A_BKR1CB065A
Synthetic calcite	RELAB	PIG004	EC-EAC-004_LAEC04
Calcite	RELAB	Calcite	GR-CMP-001_CAGR01
Calcite	RELAB	HYD-BLT-1a	HM-JFM-001_C1HM01
Calcite	RELAB	Lane calcite 63–90	JB-JLB-550_BKR1JB550
Calcite	RELAB	Lane calcite 90–125	JB-JLB-551_1101S551
Calcite	RELAB	Lane calcite 125–180	JB-JLB-552_1101S552
Calcite	RELAB	Lane calcite 180–250	JB-JLB-553_1101S553
Calcite	RELAB	Lane calcite 250–355	JB-JLB-554_1101S554
Calcite	RELAB	Lane calcite 355–500	JB-JLB-555_1101S555
Calcite	RELAB	Mazada calcite 45–75 um	JB-JLB-E57-B_BKR1JBE57B
Calcite	RELAB	Mazada calcite 75–90 um	JB-JLB-E57-C_BKR1JBE57C
Calcite	RELAB	Mazada calcite 90–125 um	JB-JLB-E57-D_BKR1JBE57D
Calcite	RELAB	Mazada calcite 125–250 um	JB-JLB-E57-E_BKR1JBE57E
Calcite	RELAB	Mazada calcite > 250 um	JB-JLB-E57-F_BKR1JBE57F
Calcite	RELAB	Big Timber calcite < 45 um	JB-JLB-E58-A_BKR1JBE58A
Calcite	RELAB	Big Timber calcite 45–75 um	JB-JLB-E58-B_BKR1JBE58B
Calcite	RELAB	Big Timber calcite 75–90 um	JB-JLB-E58-C_BKR1JBE58C
Calcite	RELAB	Big Timber calcite 90–125 um	JB-JLB-E58-D_BKR1JBE58D
Calcite	RELAB	Big Timber calcite 125–250 um	JB-JLB-E58-E_BKR1JBE58E
Calcite	RELAB	Big Timber calcite > 250 um	JB-JLB-E58-F_BKR1JBE58F
Calcite	RELAB	Red calcite	PC-CMP-055_C1PC55
Calcite	ECO-Speclib	CaCO_3	mineral.carbonate.none.coarse.tir.c-3e.jpl.nicolet
Calcite	ECO-Speclib	CaCO_3	mineral.carbonate.none.coarse.tir.calcite_1.jhu.nicolet
Calcite	ECO-Speclib	CaCO_3	mineral.carbonate.none.coarse.tir.calcite_2.jhu.nicolet
Calcite	ECO-Speclib	CaCO_3	mineral.carbonate.none.fine.tir.c-3d.jpl.nicolet
Calcite	ECO-Speclib	CaCO_3	mineral.carbonate.none.fine.tir.c-3e.jpl.nicolet
Calcite	ECO-Speclib	CaCO_3	mineral.carbonate.none.fine.tir.calcite_1.jhu.nicolet
Calcite	ECO-Speclib	CaCO_3	mineral.carbonate.none.fine.vswir.c-3a.jpl.beckman
Calcite	ECO-Speclib	CaCO_3	mineral.carbonate.none.medium.tir.c-3d.jpl.nicolet
Calcite	ECO-Speclib	CaCO_3	mineral.carbonate.none.medium.tir.c-3e.jpl.nicolet
Calcite	ECO-Speclib	CaCO_3	mineral.carbonate.none.medium.vswir.c-3a.jpl.beckman
Dolomite	RELAB	CRB103 < 45 um	CB-EAC-003-A_LACB03A
Dolomite	RELAB	CRB103 45–90 um	CB-EAC-003-B_LACB03B
Dolomite	RELAB	CRB117 < 45 um	CB-EAC-017-A_BKR1CB017A
Dolomite	RELAB	Dolomite	CC-JFM-005-B_F1CC05B
Dolomite	USGS	Dolomite HS102	Dolomite_HS102.3B_NIC4bbb_RREF
Dolomite	RELAB	Fe dolomite < 125 um	JB-JLB-779_BKR1JB779
Dolomite	RELAB	Selasvann dolomite < 45 um	JB-JLB-E61-A_BKR1JBE61A
Dolomite	RELAB	Selasvann dolomite 45–75 um	JB-JLB-E61-B_BKR1JBE61B

(continued on next page)

(*continued*)

Mineral	Source	Sample	File name
Dolomite	RELAB	Selasvann dolomite 75–90 um	JB-JLB-E61-C_BKR1JBE61C
Dolomite	RELAB	Selasvann dolomite 90–125 um	JB-JLB-E61-D_BKR1JBE61D
Dolomite	RELAB	Selasvann dolomite 125–250 um	JB-JLB-E61-E_BKR1JBE61E
Dolomite	RELAB	Selasvann dolomite > 250 um	JB-JLB-E61-F_BKR1JBE61F
Dolomite	RELAB	6521 Dolomite	SH-SJG-077_NASH77
Dolomite	RELAB	6523 Dolomite	SH-SJG-078_NASH78
Dolomite	RELAB	6528 Dolomite	SH-SJG-079_NASH79
Dolomite	RELAB	6529 Dolomite	SH-SJG-080_NASH80
Dolomite	ECO-Speclib	Dolomite CaMg(CO_3)_2	mineral.carbonate.none.coarse.tir.c-5a.jpl.nicolet
Dolomite	ECO-Speclib	Dolomite CaMg(CO3)2	mineral.carbonate.none.coarse.tir.dolomite_1.jhu.nicolet
Dolomite	ECO-Speclib	Dolomite CaMg(CO3)2	mineral.carbonate.none.coarse.tir.dolomite_2.jhu.nicolet
Dolomite	ECO-Speclib	Dolomite CaMg(CO3)2	mineral.carbonate.none.coarse.tir.dolomite_3.jhu.nicolet
Dolomite	ECO-Speclib	Dolomite CaMg(CO_3)_2	mineral.carbonate.none.fine.tir.c-5a.jpl.nicolet
Dolomite	ECO-Speclib	Dolomite CaMg(CO_3)_2	mineral.carbonate.none.fine.tir.c-5c.jpl.nicolet
Dolomite	ECO-Speclib	Dolomite CaMg(CO_3)_2	mineral.carbonate.none.medium.tir.c-5a.jpl.nicolet
Dolomite	ECO-Speclib	Dolomite CaMg(CO_3)_2	mineral.carbonate.none.medium.tir.c-5c.jpl.nicolet
Dolomite	ECO-Speclib	Dolomite CaMg(CO3)2	mineral.carbonate.none.solid.tir.dolomite_3.jhu.nicolet
Magnesite	RELAB	MGC 25–45 um	BE-JFM-223_BKR1BE223
Magnesite	RELAB	MGC 45–63 um	BE-JFM-224_BKR1BE224
Magnesite	RELAB	MGC 63–75 um	BE-JFM-225_BKR1BE225
Magnesite	RELAB	MGC 75–106 um	BE-JFM-226_BKR1BE226
Magnesite	RELAB	MGC 106–125 um	BE-JFM-227_BKR1BE227
Magnesite	RELAB	MGC 125–150 um	BE-JFM-228_BKR1BE228
Magnesite	RELAB	MGC 45–75 um	BE-JFM-231_BKR1BE231
Magnesite	RELAB	CRB106 < 45 um	CB-EAC-006-A_LACB06A
Magnesite	RELAB	CRB106 45–90 um	CB-EAC-006-B_LACB06B
Hydromagnesite	RELAB	CRB208 < 45 um	CB-EAC-028-A_LACB28A
Magnesite	RELAB	CRB144 < 45 um	CB-EAC-070-A_BKR1CB070A
Magnesite	RELAB	Brumado Bahia magnesite < 45 um	JB-JLB-946-A_BKR1JB946A
Magnesite	RELAB	Brumado Bahia magnesite 45–75 um	JB-JLB-946-B_BKR1JB946B
Magnesite	RELAB	Brumado Bahia magnesite 75–125 um	JB-JLB-946-C_BKR1JB946C
Magnesite	RELAB	Brumado Bahia magnesite < 125 um	JB-JLB-946-E_BKR1JB946E
Organic extract	Kaplan	ALH83100	ALH83100
Organic extract	Kaplan	ALH85013	ALH85013
Organic extract	Kaplan	Bells	Bells
Organic extract	Kaplan	Cold Bokkeveld	Cold Bokkeveld
Organic extract	Kaplan	GRO95566	GRO95566
Organic extract	Kaplan	GRO95577	GRO95577
Organic extract	Kaplan	LEW85311	LEW85311
Organic extract	Kaplan	MET01070	MET01070
Organic extract	Kaplan	Mighei	Mighei
Organic extract	Kaplan	Murchison	Murchison
Organic extract	Kaplan	Orgueil	Orgueil
Organic extract	Kaplan	Tag_UA_11h	Tag_UA_11h
Organic extract	Kaplan	Tagish_CCL	Tagish_CCL
Organic extract	Kaplan	Tagish_Lake	Tagish_Lake

Appendix 1 Notes:
ECOSpeclib is a JPL Facility: https://speclib.jpl.nasa.gov/library
Kaplan is: Kaplan et al., 2019.
USGS is the USGS Spectral Laboratory: https://www.usgs.gov/labs/spec-lab
RELAB is the Keck/NASA Reflectance Experiment Laboratory at Brown University: http://www.planetary.brown.edu/relab/

References

Acton, C., 1996. Ancillary data services of Nasa's Navigation and Ancillary Information Facility. Planet. Space Sci. 44 (1), 65–70.

Alexander, C.M., Fogel, M.L., Yabuta, H., Cody, G.D., 2007. The origin and evolution of chondrites recorded in the elemental and isotopic compositions of their macromolecular organic matter. Geochim. Cosmochim. Acta 71, 4380–4403.

Alexander, C.M., Cody, G.D., Kebukawa, Y., Bowden, R., Fogel, M.L., Kilcoyne, A.L.D., Nittler, L.R., Herd, C.D.K., 2014. Elemental, isotopic, and structural changes in Tagish Lake insoluble organic matter produced by parent body processes. Meteorit. Planet. Sci. 49, 503–525.

Barnouin, O.S., Daly, M.G., Palmer, E.E., Johnson, C.L., Gaskell, R.W., Al Asad, M., Bierhaus, E.B., Craft, K.L., Ernst, C.M., Espiritu, R.C., Nair, H., 2020. Digital terrain mapping by the OSIRIS-REx mission. Planet. Space Sci. 180, 104764.

Barucci, M.A., Hasselmann, P.H., Praet, A., Fulchignoni, M., Deshapriya, J.D.P., Fornasier, S., Merlin, F., Clark, B.E., Simon, A.A., Hamilton, V.E., Emery, J.P., 2020. OSIRIS-REx spectral analysis of (101955) Bennu by multivariate statistics. Astron. Astrophys. 637, L4.

Bennett, C.A., DellaGiustina, D.N., Becker, K.J., Becker, T.L., Edmundson, K.L., Golish, D. R., Lauretta, D.S., 2021. A high-resolution global basemap of (101955) Bennu. Icarus 357, 113690.

Clark, B.E., Binzel, R.P., Howell, E., Cloutis, E.A., Ockert-Bell, M.E., Christensen, P., Barucci, M.A., DeMeo, F., Lauretta, D., Connolly Jr., H., Soderberg, A., Hergenrother, C., Lim, L., 2011. Asteroid (101955) 1999 RQ36: spectroscopy from 0.4 to 2.5μm and meteorite analogs. Icarus 216, 462–475.

DellaGiustina, D.N., Burke, K.N., Walsh, K.J., Golish, D.R., Smith, P.H., Bierhaus, E.B., Becker, T., Campins, H., Tatsumi, E., Yumoto, K., Sugita, S., Prasanna Deshapriya, J. D., Cloutis, E., Clark, B.E., Hendrix, A., Sen, A., Al Asad, M., Daly, M.G., Avdellidou, C., Ballouz, R.-L., Barruci, M.A., Becker, K., Bennett, C.A., Bottke, W.F., Connolly Jr., H.C., Delbo, M., de Leon, J., Drouet d'Aubigny, C.Y., Edmundson, K.E., Fornasier, S., Hamilton, V.E., Hasselman, P., Hergenrother, C.W., Howell, E.S., Jawin, E.R., Kaplan, H.H., Le Corre, L., Lim, L., Li, J.Y., Michel, P., Molaro, J.L., Nolan, M.C., Nolau, J., Pajola, M., Popescu, M., Porter, N.A., Rizk, B., Rizos, J.L., Ryan, A.J., Rozitis, B., Simon, A.A., Trang, D., VanAuken, R.A., Wolner, C.W.V., Lauretta, D.S., 2020. Variations in color and reflectance on the surface of asteroid (101955) Bennu. Science 370. https://doi.org/10.1126/science.abc3660 eabc3660.

Deshapriya, J.D.P., Barucci, M.A., Bierhaus, E.B., Fornasier, S., Hasselmann, P.H., Merlin, F., Clark, B.E., Praet, A., Fulchignoni, M., Simon, A.A., Hamilton, V.E., Cloutis, E.A., Lantz, C., Zou, X.D., Li, J.-Y., Reuter, D.C., Brucato, J.R., Poggiali, G., Daly, R.T., Trang, D., Ferrone, S., DellaGiustina, D.N., Lauretta, D.S., 2021. Spectral analysis of craters on (101955) Bennu. Icarus 357, 114252.

Donaldson Hanna, K.L., Schrader, D.L., Cloutis, E.A., Cody, G.D., King, A.J., McCoy, T.J., Applin, D.M., Bowles, N.E., Mann, J.P., Connolly Jr., H.C., Keller, L.P., Lim, L.F., Clark, B.E., Hamilton, V.E., Lauretta, D.S., Russell, S.S., Schofield, P.F., 2019. Spectral characterization of analog samples in anticipation of OSIRIS-REx's arrival at Bennu: a blind test study. Icarus 319, 701–723.

Ferrone, S.M., Clark, B.E., Kaplan, H.H., Rizos, J.-L., Zou, X.-D., Li, J.-Y., Barucci, M.A., Simon, A., Reuter, D., Hasselman, P., Deshapriya, J.D.P., Poggiali, G., Brucato, J.R., Cambioni, S., Hamilton, V., Lauretta, D.S., 2021a. OVIRS observations of organics and carbonates on Bennu: search for surface feature context", Mendeley Data. https://doi.org/10.17632/b4b39jp8vj.1.

Ferrone, S.M., Clark, Beth E., Hawley, C. Luke, Joseph, Jonathan, Nolan, Michael C., Bennett, Carina, Zou, Xiao-Duan, Selznick, Sanford, Loveridge, Micheal, Deshapriya, Prasanna, Lauretta, Dante S., 2021b. Analysis of Projection Effects in OSIRIS-REx Spectral Mapping Methods: Recommended Protocols for Facet-Based Mapping. Earth Space Sci. 8 (3) https://doi.org/10.1029/2019EA000613 e2020EA000613.

Gazzeteer of Planetary Nomenclature. International Astronomical Union (IAU) Working Group for Planetary System Nomenclature (WGPSN), Strix Saxum. https://planetarynames.wr.usgs.gov/Feature/15886;jsessionid=9F4BCD10B109213D138C210D5183A57C.

Glavin, D.P., Alexander, C.M., Aponte, J.C., Dworkin, J.P., Elsila, J.E., Yabuta, H., 2018. The origin and evolution of organic matter in carbonaceous chondrites and links to their parent bodies. In: Primitive Meteorites and Asteroids. Elsevier, the Netherlands, pp. 205–271 edited by Abreu N. Amsterdam.

Golish, D.R., d'Aubigny, C.D., Rizk, B., DellaGiustina, D.N., Smith, P.H., Becker, K., Shultz, N., Stone, T., Barker, M.K., Mazarico, E., Tatsumi, E., 2020. Ground and in-flight calibration of the OSIRIS-REx camera suite. Space Sci. Rev. 216 (1), 12.

Golish, D.R., DellaGiustina, D.N., Li, J.-Y., Clark, B.E., Zou, X.-D., Smith, P.H., Rizos, J.L., Hasselmann, P.H., Bennett, C.A., Fornasier, S., Ballouz, R.-L., Drouet d'Aubigny, C., Rizk, B., Daly, M.G., Barnouin, O.S., Philpott, L., Al Asad, M.M., Seabrook, J.A., Johnson, C.L., Lauretta, D.S., 2021. Disk-resolved photometric modeling and properties of asteroid (101955) Bennu. Icarus 357, 113724. https://doi.org/10.1016/j.icarus.2020.113724.

Hamilton, V., Simon, A.A., Christensen, P.R., Reuter, D.C., Clark, B.E., Barucci, M.A., Bowles, N.E., Boynton, W.V., Brucato, J.R., Cloutis, E.A., Connolly Jr., H.C., Donaldson Hanna, K.L., Emery, J.P., Enos, H.L., Fornasier, S., Haberle, C.W., Hanna, R.D., Howell, E.S., Kaplan, H.H., Keller, L.P., Lantz, C., Li, J.-Y., Lim, L.F., McCoy, T.J., Merlin, F., Nolan, M.C., Praet, A., Rozitis, B., Sandford, S.A., Schrader, D.L., Thomas, C.A., Zou, X.-D., Lauretta, D.S., The OSIRIS-REx Team, 2019. Evidence for hydrated minerals on asteroid (101955) Bennu. Nat. Astron. 3, 332–340.

Hunter, J.D., 2007. Matplotlib: a 2D graphics environment. Comput. Sci. Eng. 9 (3), 90–95. https://doi.org/10.5281/zenodo.592536.

Kaplan, H.H., Milliken, R.E., Alexander, C.M.O.D., Herd, C.D., 2019. Reflectance spectroscopy of insoluble organic matter (IOM) and carbonaceous meteorites. Meteorit. Planet. Sci. 54 (5), 1051–1068.

Kaplan, H.H., Lauretta, D.S., Simon, A.A., Hamilton, V.E., DellaGiustina, D.N., Golish, D. R., Reuter, D.C., Bennett, C.A., Burke, K.N., Campins, H., Connolly, H.C., 2020a. Bright carbonate veins on asteroid (101955) Bennu: implications for aqueous alteration history. Science 370 eabc3557.

Kaplan, H.H., Hamilton, V.E., Howell, E.S., Scott Anderson, F., Barrucci, M.A., Brucato, J., Burbine, T.H., Clark, B.E., Cloutis, E.A., Connolly Jr., H.C., Dotto, E., 2020b. Visible–near infrared spectral indices for mapping mineralogy and chemistry with OSIRIS-REx. Meteorit. Planet. Sci. 55 (4), 744–765. https://doi.org/10.1111/maps.13461.

Lauretta, D.S., Balram-Knutson, S.S., Beshore, E., Boynton, W.V., Drouet d'Aubigny, C., DellaGiustina, D.N., Enos, H.L., Golish, D.R., Hergenrother, C.W., Howell, E.S., Bennett, C.A., Morton, E.T., Nolan, M.C., Rizk, B., Roper, H.L., Bartels, A.E., Bos, B. J., Dworkin, J.P., Highsmith, D.E., Lorenz, D.A., Lim, L.F., Mink, R., Moreau, M.C., Nuth, J.A., Reuter, D.C., Simon, A.A., Bierhaus, E.B., Bryan, B.H., Ballouz, R., Barnouin, O.S., Binzel, R.P., Bottke, W.F., Hamilton, V.E., Walsh, K.J., Chesley, S.R., Christensen, P.R., Clark, B.E., Connolly, H.C., Crombie, M.K., Daly, M.G., Emery, J. P., McCoy, T.J., McMahon, J.W., Scheeres, D.J., Messenger, S., Nakamura-Messenger, K., Righter, K., Sandford, S.A., 2017. OSIRIS-REx: sample return from asteroid (101955) Bennu. Space Sci. Rev. 212 (1–2), 925–984.

Lauretta, D.S., Enos, H.L., Polit, A.T., Roper, H.L., Wolner, C.W.V., 2021. OSIRIS-REx at Bennu: overcoming challenges to collect a sample of the early solar system. In: Longobardo, A. (Ed.), Sample Return Missions. Elsevier (chapter 8).

MATLAB, 2010. Version 9.7.0.1296695 (R2019b) Update 4. The MathWorks Inc., Natick, Massachusetts.

McEwen, A.S., 1991. Photometric functions for photoclinometry and other applications. Icarus 92 (2), 298–311.

McKinney, W., et al., 2010. Data structures for statistical computing in python. In: Proceedings of the 9th Python in Science Conference, Vol. 445, pp. 51–56.

Moroz, L., Baratta, G., Strazzulla, G., Starukhina, L., Dotto, E., Barucci, M.A., Distefano, E., 2004. Optical alteration of complex organics induced by ion irradiation:: 1. Laboratory experiments suggest unusual space weathering trend. Icarus 170 (1), 214–228.

Paclik, P., Duin, R.P., 2003. Dissimilarity-based classification of spectra: computational issues. Real-Time Imag. 9 (4), 237–244.

Pieters, C.M., Hiroi, T., 2004. RELAB (Reflectance Experiment Laboratory): a NASA Multiuser Spectroscopy Facility. 35th Lunar and Planetary Science Conference, March 15-19, 2004, League City, Texas, LPI abstract no.1720.

Praet, A.M., Barucci, A., Clark, B.E., Kaplan, H.H., Simon, A.A., Hamilton, V.E., Emery, J. P., Howell, E.S., Lim, L.F., Zou, X.-D., Li, J.-Y., Reuter, D.C., Merlin, F., Deshapriya, J. D.P., Fornasier, S., Hasselmann, P.H., Poggiali, G., Ferrone, S., Brucato, J.R., Takir, D., Cloutis, E., Connolly Jr., H.C., Fulchignoni, M., Lauretta, D.S., 2020. Hydrogen Abundance Estimation and Distribution on (101955) Bennu. Icarus 363, 114427. https://doi.org/10.1016/j.icarus.2021.114427.

Price-Whelan, A.M., Sipőcz, B.M., Günther, H.M., Lim, P.L., Crawford, S.M., Conseil, S., Shupe, D.L., Craig, M.W., Dencheva, N., Ginsburg, A., VanderPlas, J.T., 2018. The Astropy project: building an open-science project and status of the v2. 0 core package. Astron. J. 156 (3), 123.

Reuter, D.C., Simon, A.A., Hair, J., Lunsford, A., Manthripragada, S., Bly, V., Bos, B., Brambora, C., Caldwell, E., Casto, G., Dolch, Z., 2018. The OSIRIS-REx visible and InfraRed spectrometer (OVIRS): spectral maps of the asteroid Bennu. Space Sci. Rev. 214 (2), 54.

Reuter, D.C., Simon, A.A., Lunsford, A., Lauretta, D.S., 2019. Origins, Spectral Interpretation, Resource Identification, Security, Regolith Explorer (OSIRIS-REx): Visible and InfraRed Spectrometer (OVIRS) Bundle, NASA Planetary Data System, urn:nasa:pds:orex.ovirs.

Rizk, B., Drouet d'Aubigny, C., Golish, D., Fellows, C., Merrill, C., Smith, P., Walker, M. S., Hendershot, J.E., Hancock, J., Bailey, S.H., DellaGiustina, D.N., Lauretta, D.S., Tanner, R., Williams, M., Harshman, K., Fitzgibbon, M., Verts, W., Chen, J., Connors, T., Hamara, D., Dowd, A., Lowman, A., Dubin, M., Burt, R., Whiteley, M., Watson, M., McMahon, T., Ward, M., Booher, D., Read, M., Williams, B., Hunten, M., Little, E., Saltzman, T., Alfred, D., O'Dougherty, S., Walthall, M., Kenagy, K., Peterson, S., Crowther, B., Perry, M.L., See, C., Selznick, S., Sauve, C., Beiser, M., Black, W., Pfisterer, R.N., Lancaster, A., Oliver, S., Oquest, C., Crowley, D., Morgan, C., Castle, C., Dominguez, R., Sullivan, M., 2018. OCAMS: the OSIRIS-REx camera suite. Space Sci. Rev. 214, 26.

Rizk, B., Drouet d'Aubigny, C., Golish, D., DellaGiustina, D.N., Lauretta, D.S., 2019. Origins, Spectral Interpretation, Resource Identification, Security, Regolith Explorer (OSIRIS-REx): OSIRIS-REx Camera Suite (OCAMS) Bundle, NASA Planetary Data System, urn:nasa:pds:orex.ocams.

Rizos, J.L., de León, J., Licandro, J., Golish, D.R., Campins, H., Tatsumi, E., Popescu, M., DellaGiustina, D.N., Pajola, M., Li, J.-Y., Becker, K.J., Lauretta, D.S., 2021. Bennu's global surface and two candidate sample sites characterized by spectral clustering of OSIRIS-REx multispectral images. Icarus 364, 114467.

Robitaille, T.P., Tollerud, E.J., Greenfield, P., Droettboom, M., Bray, E., Aldcroft, T., Davis, M., Ginsburg, A., Price-Whelan, A.M., Kerzendorf, W.E., Conley, A., 2013. Astropy: a community Python package for astronomy. Astron. Astrophys. 558, A33.

Simon, A.A., Reuter, D.C., Gorius, N., Lunsford, A., Cosentino, R.G., Wind, G., Lauretta, D.S., 2018. In-flight calibration and performance of the OSIRIS-REx visible and IR spectrometer (OVIRS). Remote Sens. 10 (9), 1486.

Simon, A., Kaplan, H.H., Hamilton, V.E., Lauretta, D.S., Campins, H., Emery, J.P., Barucci, M.A., DellaGiustina, D.N., Reuter, D.C., Sandford, S.A., Golish, D.R., Lim, L. F., Ryan, A., Rozitis, B., Bennett, C.A., 2020a. Widespread carbon-bearing materials on near-Earth asteroid (101955) Bennu. Science 370 eabc3522.

Simon, A., Kaplan, H.H., Cloutis, E., Hamilton, V.E., Lantz, C., Reuter, D.C., Trang, D., Fornasier, S., Clark, B.E., Lauretta, D.S., 2020b. Weak spectral features on (101995) Bennu from the OSIRIS-REx visible and InfraRed spectrometer. Astron. Astrophys. 644, A148.

Van der Walt, Stéfan, Colbert, S. Chris, Varoquaux, Gaël, 2011. The NumPy array: a structure for efficient numerical computation. Comput. Sci. Eng. 13, 22–30.

Walsh, K.J., Jawin, E.R., Ballouz, R.L., Barnouin, O.S., Bierhaus, E.B., Connolly, H.C., Molaro, J.L., McCoy, T.J., Delbo, M., Hartzell, C.M., Pajola, M., 2019. Craters, boulders and regolith of (101955) Bennu indicative of an old and dynamic surface. Nat. Geosci. 12 (4), 242–246.

Zou, X.D., Li, J.Y., Clark, B.E., Golish, D.R., Ferrone, S.M., Simon, A.A., Reuter, D.C., Domingue, D.L., Kaplan, H.H., Barucci, M.A., Fornasier, S., Praet, A., Hasselmann, P. H., Bennett, C., Cloutis, E.A., Tatsumi, E., DellaGiustina, D.N., Lauretta, D.S., 2021. Photometry of asteroid (101955) Bennu with OVIRS on OSIRIS-REx. Icarus 358, 114183.